1   **Imprint of minute hydrocarbon seepage on solid phase and pore water**

2   **geochemistry in organic-poor subseafloor sediment**

3   Ellen Schnabel[1]*, Jessica Stammeier[2], Stefanie Poetz[3], Kai Mangelsdorf[3], Aurèle Vuillemin[1],
4   Rolando di Primio[4], Jens Kallmeyer[1], the PROSPECTOMICS Consortium

5   [1]GFZ Helmholtz Centre for Geosciences, Section Geomicrobiology, Telegrafenberg, 14473
6   Potsdam, Germany

7   [2]GFZ Helmholtz Centre for Geosciences, Section Inorganic and Isotope Geochemistry,
8   Telegrafenberg, 14473 Potsdam, Germany

9   [3]GFZ Helmholtz Centre for Geosciences, Section Organic Geochemistry, Telegrafenberg,
10   14473 Potsdam, Germany

11   [4]AkerBP, 1366 Lysaker, Norway

12   *Corresponding author: MSc Ellen Schnabel, eschnabe@gfz.de

13   Keywords: hydrocarbon seepage; reductive diagenesis; authigenic minerals; microbial
14   activity; Barents Sea; sediment biogeochemistry

Key Points

16   • Even inconspicuous hydrocarbon seepage modifies redox zonation and stimulates
17   carbonate and sulfide mineral formation in marine sediments.
18   • Subtle seepage causes distinct spatial heterogeneity in pore water chemistry and
19   mineral formation patterns.
20   • Authigenic minerals and pore water gradients serve as complementary indicators of
21   past and ongoing seepage.

Abstract

23   In marine environments, small hydrocarbon (HC) fluxes through organic-poor sediments are

24   often fully degraded by microorganisms before reaching the seabed. Yet, these fluxes

25   influence sediment geochemistry by stimulating microbial activity. We analyzed 50 gravity

26   cores from the southwestern Barents Sea, covering zones affected by inconspicuous HC

27   seepage and unaffected reference zones. Using various organic and inorganic geochemical

28 analyses of the sediment along with pore water geochemistry, we assess the effects of low-

29 intensity seepage and identify potential geochemical signatures.

30 While analysis of the organic geochemical analyses provided limited insights, inorganic

31 geochemical analyses revealed formation of minerals such as carbonates and sulfides, linked

32 to microbial reductive processes. Element concentrations suggested that HC degradation

33 leaves distinct signatures, particularly in redox-sensitive minerals. Pore water profiles in HC-

34 affected zones showed significant variation, indicating carbonate precipitation. In contrast,

35 sediments not affected by HC seepage displayed more uniform pore water profiles.

36 Estimated fluxes of sulfate, calcium, and alkalinity varied notably between cores, particularly

37 in HC-affected zones, suggesting local and potentially transient differences in seepage

38 intensity.

39 While microbial HC degradation likely occurs deeper than our sampling interval, high-

40 resolution geochemical analysis of both sediment fractions and pore water revealed a clear

41 imprint of HC seepage. This imprint, reflected in authigenic minerals and pore water

42 gradients, allows identification of past and present seepage activity, with authigenic

43 minerals providing evidence for past seepage, and pore water profiles informing about

44 ongoing seepage.

45 **Plain language summary**

46 Hydrocarbons like methane or oil can naturally seep from underground reservoirs into

47 marine sediments. Often, this seepage is so small that hydrocarbons are fully degraded by

48 microorganisms before they reach the upper sediment layers near the seafloor.

49 In this study, we analyzed sediment from the southwestern Barents Sea, a region with very

50 low natural organic content, to investigate whether such subtle hydrocarbon seepage leaves

51 detectable traces, even when hydrocarbons are already consumed below the depth we

52 sampled.

53 Our results show that despite the complete degradation of hydrocarbons deeper in the

54 sediment, distinct changes in pore water chemistry and mineral composition persist in the

55 upper layers. We observed variations in sulfate, calcium, and alkalinity profiles, along with

56 the formation of minerals like carbonates and sulfides.

57 These findings reveal that even low-intensity hydrocarbon seepage can leave a long-lasting

58 imprint in sediments, not only through direct hydrocarbon presence, but also through their

59 impact on geochemical processes. This insight helps improving the detection of past or

60 ongoing seepage in marine environments and supports a better understanding of

61 biogeochemical cycles below the seafloor.

62 **1. Introduction**

63 Marine subseafloor biogeochemical cycles are primarily governed by microorganisms (Joye

64 et al., 2022), their metabolic activity is strongly controlled by availability and reactivity of

65 sedimentary organic substrates. Due to lesser primary productivity of surface waters as

66 compared to coastal areas (Chavez et al., 2011), in offshore sediments bioavailable organic

67 matter (OM) is typically limited and becomes more recalcitrant with burial depth

68 (Middelburg, 2018) due to lower sedimentation rates (Røy et al., 2012). However, as all

69 hydrocarbon reservoirs leak to some degree (Hunt, 1995; Heggland, 1998; Yergin, 2009),

70 underlying hydrocarbon reservoirs will lead to buoyant hydrocarbon-rich fluids migrating

71 upwards through the sediment column (Ciotoli et al., 2020). These HCs, even in trace

72 amounts, represent an additional electron donor that can significantly fuel microbial activity

73 (Zhang et al., 2022). Such influx of labile OM (i.e. seepage) leads to changes in microbial

74 communities in terms of diversity and activity, which affect in turn specific physicochemical

75 properties of the sediment, such as porosity, density, pore water geochemistry and mineral

76 composition, (Abrams, 2005; Hvoslef et al., 1996; Joye, 2020). HC seepage through marine

77 sediments fuels a variety of microbial processes, including sulfate reduction, fermentation,

78 and methanogenesis (Joye, 2020; Schnabel et al., 2025). Although these microbial processes

79 are central to *in situ* biogeochemical transformations of OM on the continental shelf

80 (Bradley et al., 2020), they are less pronounced in pelagic sediments wherein sulfate

81 reduction becomes limited due to energy limitation (Vuillemin et al., 2020).Thus, at sites

82 with low seepage rates HCs may be fully mineralized before reaching the sediment surface.

83 Nevertheless, subtle but continuous HC fluxes influence sediment geochemistry and

84 microbiology, not only in the direct vicinity of the HC source but also extending to the

85 sediment surface (Rasheed et al., 2013; Joye et al., 2004).

86   Dissimilatory sulfate reduction (DSR), which is the predominant terminal electron-accepting

87   pathway in oxygen-depleted, sulfate-containing shallow marine sediments (Kasten and

88   Jørgensen, 2000; Bowles et al., 2014; Jørgensen et al., 2019), can be expected to be

89   influenced by HC seepage and potentially be key in defining HC-related reductive diagenesis

90   (Joye et al., 2004). Organoclastic sulfate reduction (OSR) relies on low molecular weight

91   substrates derived from fermented particulate or dissolved OM (Jørgensen, 1982), whereas

92   methanotrophic sulfate reduction is performed in conjunction with methane-oxidizing

93   archaea (ANME) during anaerobic oxidation of methane (AOM) (Orphan et al., 2001). Thus,

94   the influence of HC seepage on sulfate-reducing bacteria (Widdel et al., 2010) highly

95   depends on whether light (i.e. gaseous, soluble) or heavy (i.e. long chain alkanes, aromatic

96   rings) HCs are supplied. The types of seeping HCs and their subsequent microbial alteration

97   can be resolved using mass spectrometry of sediment organic extracts, e.g. a shift from

98   polar to less polar unsaturated HCs is observed during maturation (Hu et al., 2023), whereas

99   the loss of hydrogen atoms in alkanes (via dehydrogenation) or oxygen incorporation in

100   aromatic rings (cleavage via hydroxylation) reveal subsequent microbial alteration (Sert et

101   al., 2020). Further geochemical effects inherent to sulfate reduction (SR) include an increase

102   in pore water alkalinity, primarily as dissolved inorganic carbon (DIC) in the form of

103   bicarbonate (HCO_3^-), and production of hydrogen sulfide (H_2S). Together these metabolic

104   solutes create favorable sedimentary conditions for the precipitation of carbonate and

105   sulfide minerals (Berner, 1981; Hinrichs et al., 1999; Lin et al., 2016), namely calcite ($CaCO_3$),

106   mackinawite (FeS) and pyrite (FeS_2). Carbonates can record redox conditions at the time of

107   formation (Vuillemin et al., 2023a and 2023b) while their trace element compositions can

108   indicate progressive alteration or diagenesis (Smrzka et al., 2019), in particular redox-

109   sensitive trace metals (Smrzka et al., 2020; Tribovillard et al., 2013). Similarly, iron sulfides

110   scavenge specific trace elements from the pore water (Huerta-Diaz and Morse, 1992),

111   including chalcophilic and redox-sensitive bioessential metals (e.g., Mn, Mo, Cu, Zn).

112   Local redox conditions mediated by microbial processes also affect HC mobility as they

113   promote the formation (e.g. carbonates) or dissolution (e.g. clays) of mineral barriers that

114   adsorb HCs or impede their diffusion (Zhao et al., 2024; Eichhubl et al., 2009). For instance,

115   the transition of smectite to illite— decreases the mineral swelling capacity and reduces

116   permeability (Kim et al., 2004; Dong et al., 2009). Such interplay of physical, geochemical

117 and biological factors affects the migration of HCs and generates complex but characteristic

118 flow patterns at active seep systems (De Groot et al., 2024). Thus, seep systems are

119 characterized by pronounced spatial and temporal variations, permeability, fluid flow

120 dynamics, and pressure conditions governing the rate at which HCs migrate upward (Foster

121 et al., 2015; Leifer et al., 2004; De Groot et al., 2024), reasons for which characteristic HC

122 seeps ~~are~~can be classified according to flux and surface manifestations (Table 1). {Note that

123 some seep-features like e.g. carbonate crusts or pockmarks remain even after active

124 seepage stopped (Nickel~~, 2013 #472;~~ et al. 2012, Nickel~~, 2012 #29}~~ et al. 2013).

125 **Table 1.** Classification of hydrocarbon seeps based on methane flux and associated surface manifestations. The

126 table is compiled after (Judd and Hovland (2009); Etiope (2015). The flux range between inconspicuous- and

127 moderate-flux seeps (1 mmol × m² × d⁻¹ to 100 mmol × m² × d⁻¹) represents a conceptual transition zone,

128 where current data are insufficient to establish a clear distinction.

Seep type	~~Low flux~~Inconspicuous seeps	Moderate seeps	High flux seeps
Flux range	< 1 mmol × m² × d⁻¹	0.1–1 mol × m² × d⁻¹	1–10 mol × m² × d⁻¹
Pockmarks	No pockmarks	Small, less deeply pronounced pockmarks	Larger, deeper and more numerous pockmarks, clearer
Methane and gas bubbles	No bubbles	Few, smaller bubbles, mostly sporadic	Frequent and larger bubbles, continuous gas flow
Chemical changes	No or minimal chemical changes on the surface	Low concentration of carbonates and sulfides	Significant enrichment of carbonates and sulfides, possible mineral deposits
Biogenic hotspots	No biological hotspots	Local colonization of methane-oxidizing bacteria	Intensive biological activity, larger hotspots with more diverse methane-fed fauna (e.g. mussels)
Gas hydrates	No gas hydrates	Little or no gas hydrates	Possible presence of gas hydrates, especially at low temperatures and high methane flow

129 ~~Because~~According to our definition inconspicuous HC ~~seepage lacks clear~~seeps are seeps

130 where the seeping HCs lack visible surface manifestations~~, related diffusive~~. Instead, the HCs

131 spread diffusely and are used up by biogeochemical processes~~, although~~ so that the HCs do

132 not reach the SWI. Although they likely ~~to~~imprint sediment geochemistry, they often

133 remain undetected. Yet, any additional energy flux from weak seepage tends to promote

134 complex interactions among local microbial communities adapted to substrate limitation or

135 not, and influence the sediment geochemical dynamics, leading to fundamental metabolic

136 and diagenetic processes (Abrams, 2020).

137 Here, we investigate how subtle, inconspicuous HC seepage influences the geochemical

138 composition of both pore water and sediment. We analyzed 50 gravity cores ~~up to 3~~

139 ~~meters in length~~ collected from the southwestern Barents Sea, including 40 cores from

140 zones affected by low-intensity seepage and 10 from unaffected reference zones. ~~This~~Given

141 the challenges of deeper coring and the goal of minimizing environmental impact, we

142 focused on the upper 3 meters of sediment to determine whether direct or indirect effects

143 of seepage could be detected. The large number of cores allows us to identify small-scale

144 geochemical patterns and evaluate any spatial heterogeneity of discrete infiltrations. By

145 combining organic and inorganic analyses of the sediment with pore water geochemistry,

146 we decipher (I) the extent to which inconspicous HC seeps affect the distribution of key

147 geochemical species (e.g. sulfide, methane, calcium, alkalinity) in pore water and sediment,

148 and (II) how these parameters vary spatially across and between seepage and reference

149 zones.

150 **2. Material and Methods**

151 **2.1. Geological setting and sampling**

152 The Barents Sea is an epicontinental shelf sea bordered by the Norwegian Sea to the

153 southwest, the Arctic Ocean to the north, and the Russian archipelago of Novaya Zemlya to

154 the east. It rests on a Caledonian basement formed during Paleozoic orogenies, but its

155 present structural configuration mainly reflects Mesozoic and Cenozoic tectonic phases,

156 including episodes of uplift, subsidence, tilting, and erosion. This has resulted in a varied

157 structural landscape with elevated highs (e.g., the Loppa High) and intervening sedimentary

158   basins (Doré, 1995; Gabrielsen et al., 1990; Johansen et al., 1993; Larssen et al., 2002;

159   Faleide et al., 1984). During the Mesozoic, organic-rich marine shales were deposited under

160   greenhouse climate conditions with high marine productivity and fluctuating sea levels.

161   These shales—particularly the Upper Jurassic Hekkingen Formation, act as the principal

162   source rocks for hydrocarbons in the southwestern Barents Sea (Marín et al., 2020; Langrock

163   et al., 2003). Burial over millions of years led to thermal maturation, hydrocarbon

164   generation, and subsequent migration into structural traps, such as those found in the

165   Johan Castberg and Snøhvit fields. In the Quaternary, the region was repeatedly covered by

166   ice sheets. During the last glaciation, the Barents Sea was overridden by grounded ice,

167   leading to significant glacial erosion. Consequently, the modern sediment cover on

168   structural highs is often very thin and sediments primarily consist of glacial and glaciomarine

169   silty clays, dropstones, and fine sands derived from the erosion of local and distal bedrock

170   during glacial advance and retreat. These surficial sediments are typically organic-poor,

171   reflecting both their glacial origin and limited biological productivity during deposition

172   (Knies and Martinez, 2009; Nickel et al., 2013; Sættem et al. (1991); Elverhøi and Solheim

173   (1983).
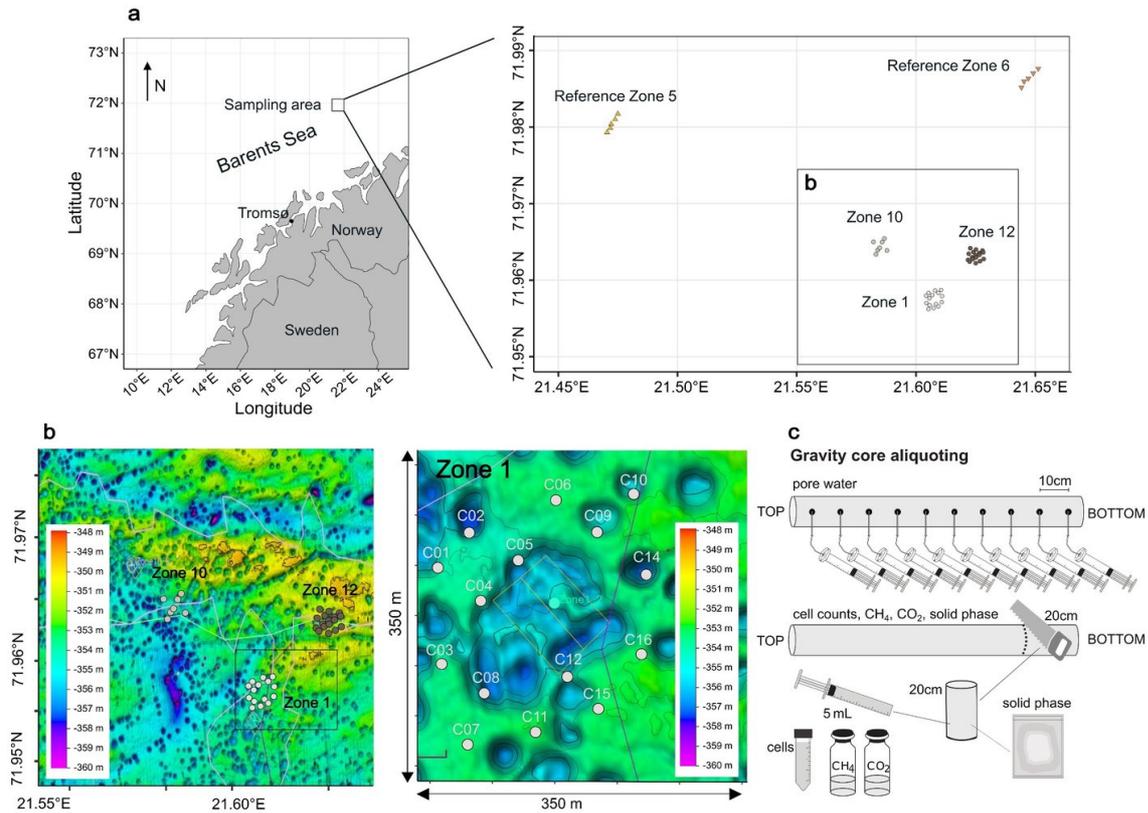
174
175 **Figure 1. Sampling locations.** (a) Map of the Norwegian coast. The square marks the sampling area. Fifty cores
176 were retrieved from three HC-affected zones (Zone 1, Zone 10, Zone 12) and two reference zones (Ref 5, Ref
177 6). (b) Bathymetric map of the 3 HC-affected zones. Each zone was sampled in a grid of cores, Zone 1 is
178 enlarged here as an example. The missing samples in the middle are due to the increased occurrence of
179 dropstones in this area, preventing the deployment of a gravity corer. (c) Schematic overview of the sampling
180 strategy. This figure was modified after (Schnabel et al., 2025)

181 During an expedition to the SW Barents Sea in Oct/Nov 2021, we collected a total of fifty
182 gravity cores, ranging from 0.5 to 3 meters in length, within three zones with known
183 underlying HC reservoirs (Z01, Z10, Z12), as well as two zones (Ref5, Ref6) with no HC
184 reservoirs, labelled hereafter as HC zones and reference zones (Fig. 1a). The coring sites lie
185 at a water depth of approximately 350 meters (Fig. 1b). Immediately after retrieval of a
186 core (Fig. 1c), the lowermost 20 cm of the core were cut off, the sediment was pushed out
187 of the liner and the outer 1-2 cm were scraped off with a sterile spatula to remove possible
188 contamination. Using 5 mL cut-off syringes, 3 cm^3 of sediment were transferred into a 10 mL
189 glass crimp vial containing saturated NaCl solution. The vials were immediately sealed with
190 thick butyl rubber stoppers, crimped, and stored upside down without headspace until
191 ~~analysis~~gas analyses in the home lab. An additional 2 cm³ of sediment was transferred into a

192   15 mL centrifuge tube containing 8 mL of NaCl-formalin fixative solution (25 g × L^{-1} NaCl, 20

193   g × L^{-1} formalin) and thoroughly homogenized for cell counting. The remaining sediment was

194   aliquoted for solid phase geochemistry. The rest of the core was cut into 1 m sections,

195   capped and stored on deck, as air, water and sediment temperature were all around 5 °C.

196   Pore water was extracted on board, with extractions ~~started~~initiated within two hours of

197   core retrieval ~~of the cores~~. Rhizon pore water samplers (Rhizosphere Research Products

198   B.V., Netherlands; (Seeberg-Elverfeldt et al., 2005)) were inserted into the intact sediment

199   core through small holes drilled in ca. 10 cm intervals. Pore water collection took between

200   12 and 24 hours. The collected pore water samples were 0.22 μm- filtered (Merck Millex™-

201   GS Sterile Syringe Filter Unit, MCE) and aliquoted for different downstream analyses. For

202   anion, cation, and trace element measurements, 1.5 mL each was collected in plastic screw-

203   cap vials without any further treatment. These samples were kept anoxic until analysis. For

204   alkalinity measurements, 2 mL of pore water were filled into a glass vial pre-filled with 50 μL

205   of saturated $HgCl_2$ solution to prevent bacterial activity (Edenborn et al., 1985) and closed

206   without any headspace. For quantification of dissolved hydrogen sulfide, we transferred 1.5

207   mL of pore water into a 2 mL plastic screw-cap vial and added 200 μL $ZnCl_2$ (20 % weight ×

208   vol^{-1}). All samples were stored at +4 °C until analysis in the home lab.

209   **2.2. Methane and carbon dioxide concentrations**

210   Prior to measurement, we introduced 3 mL of ultrapure helium gas as headspace while

211   withdrawing the same amount of NaCl solution from the crimped vial. To equilibrate

212   dissolved gases with the headspace, the content of the vials was mixed at 220 rpm on an

213   orbital shaker for 18 h, and further vortexed to break up the remaining small clayey

214   aggregates. A 250 μL sample of the headspace gas was then extracted and introduced into a

215   7890A Gas Chromatography System, which was equipped with both a flame ionization

216   detector (FID) and a thermal conductivity detector (TCD), along with an HP PLOT Q column

217   (all from Agilent). The oven temperature was set to 50 °C, the flow rate was maintained at

218   17.2 mL min^{-1}, and the pressure was held at 13 psi. Both detectors operated at 200 °C with

219   flow rates of 40 mL min^{-1} (FID) and 15 mL min^{-1} (TCD). Calibration of the system was

220   performed by injecting pure analytical standards with CO_2 concentrations of 310 ppm and

221 5270 ppm, as well as CH_4 concentrations of 10 ppm and 5170 ppm. The initial CH_4 and CO_2

222 concentrations were converted from ppm to molar concentrations using the ideal gas law.

2.3. Cell counting

224 Total cell counts were conducted following a protocol based on Kallmeyer et al. (2008).

225 Sediment samples were initially diluted at a ratio of 1:100 using a 25 g L^{-1} NaCl solution. 25

226 µL of the resulting slurry were uniformly distributed onto black 0.2 µm polycarbonate

227 Cyclopore membrane filters (Whatman International Ltd, Maidstone, UK) via vacuum

228 filtration. For cell visualization, filters were stained with a mixture consisting of SYBR Green I

229 (10 µL; Molecular Probes, Eugene, USA), phenylenediamine (100 µL), glycerol (300 µL), Milli-

230 Q water (300 µL), and 300 µL of VECTASHIELD® Antifade Mounting Medium (H-1000-10,

231 Vector Laboratories, Burlingame, USA). A volume of 15 µL of this staining solution was

232 applied to each filter. The counting was performed using an epifluorescence microscope

233 (Leica DM2000, Wetzlar, Germany) by counting cells in 200 fields of view. Cell abundances

234 were calculated as log_{10} cells per cm³ of sediment, based on triplicate measurements, with

235 standard deviations consistently remaining below 15%.

2.4. Pore water geochemistry

237 Dissolved sulfate was quantified via suppressed Ion Chromatography (column: SykroGel A ×

238 300 AB-A01; eluent: 7.3 mg L^{-1} NaSCN and 636 mg L^{-1} $NaCO_3$; pump rate 1 mL min^{-1};

239 injection volume 50 µL). The detection limit was 5 µM. Samples were measured in triplicate,

240 with average relative standard deviations consistently below 3%.

241 Cation and trace elemental concentrations in the pore water were determined using high-

242 resolution inductively coupled plasma mass spectrometry (HR-ICP-MS, ELEMENT 2XR,

243 Thermo Scientific, Waltham, USA) at the ElMiE-labs at GFZ. Prior to analysis, after acidifying

244 the samples with ultrapure HNO_3. Until analysis, the samples were kept anoxic to prevent

245 precipitation and potential alteration of the metal concentrations. 100 µL of pore water was

246 doped with 10 µL of an indium (In) standard solution at a concentration of 100 µg L^{-1} and

247 the samples where diluted with 2 vol% ultrapure HNO_3. Trace elements were quantified by

248 external calibration using single-element standards, carefully matched to the sample matrix.

249 The acid blank was subtracted from each measurement. The detection limits for the applied

250   ICP-MS routine typically ranged between 0.5 and 1 ng g^{-1}, for the analytes. Measurement

251   uncertainty, referring to the repeatability of the measurements, was about 2-5 % for all

252   analyses.

253   Iron concentrations were analyzed separately using spectrophotometry, following the

254   protocol described by Viollier et al. (2000). The detection limit of this method is 0.25 µM

255   and the measurement uncertainty was approximately 5 % for all analyses. Sulfide was

256   determined photometrically according to Cline (1969). The detection limit is 0.1 µM. All

257   samples were measured in triplicates and the results were averaged with a standard

258   deviation ≤ 3.5 %. Alkalinity was determined via titration using the Visocolor HE alkalinity AL

259   7 kit (Macherey-Nagel GmbH) adapted to the sample volume of 500 µL. The detection limit

260   is 0.15 mM and triplicate measurements differed by less than 3 %.

261   **2.5. Sediment inorganic fraction**

262   For XRF analysis, approximately 30 g of sediment material was freeze-dried, ground in agate

263   mortars using a Fritsch Pulverisette 5 planetary mill at 300 rpm for 5 minutes, sieved

264   through a 63 µm stainless steel mesh, and then melted with two Fluxana reference

265   materials to form glass discs. These discs were analyzed using an AXIOS X-ray fluorescence

266   (XRF) advanced spectrometer (Malvern Panalytical, United Kingdom), equipped with an End-

267   window RH X-ray tube SST-mAX at a 4 kW output. Elemental proportions were determined

268   for major elements as oxides in weight % [wt %] (i.e. SiO_2, Al_2O_3, Fe_2O_3, MnO, MgO, CaO,

269   Na_2O, K_2O, P_2O_5, TiO_2, SO_3, loss on ignition (LOI)), and trace elements [ppm] (i.e. Ba, Cr, Zn,

270   Ga, Nb, Ni, Rb, Sr, V, Y, Zr). Quantification limits for major elements were 0.02 wt % and

271   approximately 10 ppm for trace elements. LOI was determined based on the mass

272   difference before and after fusion. Reproducibility was evaluated using reference materials

273   and better than 2% for all major elements.

274   **2.6. Statistical and geostatistical analyses**

275   Min-max normalization was applied to the XRF dataset, scaling all variables to a range

276   between 0 and 1. PCA was then performed using the prcomp() function in R with centering

277   and scaling enabled to identify patterns and relationships among chemical species in the

278   solid sediment phase, reducing the data's dimensionality and highlighting key variability

279 across samples. This analysis provided further insight into the underlying structure of the

280 data, complementing the subsequent visualizations. For ternary visualization, selected

281 standardized parameters were then proportionally scaled to sum to 100 %. In some cases,

282 the resulting values of multiple compounds (e.g., those associated with specific mineral

283 groups like carbonates) were summed. Thus, the ternary diagrams reflect only relative

284 patterns and should not be interpreted in terms of absolute abundances.

285 We applied Mann–Whitney U tests (Mann and Whitney, 1947) using the function

286 *wilcox.test()* to XRF and pore water data to assess whether the median values of individual

287 chemical species differed significantly between groups. This non-parametric test was used

288 to evaluate differences in concentration gradients in the pore water and absolute

289 concentrations in the solid sediment phase between HC-affected zones (Z01, Z10, Z12) and

290 reference sites (Ref5, Ref6), as well as among and within individual zones and sediment

291 cores. To assess differences in variability (i.e. variance), we also used the Brown-Forsythe

292 test (Brown and Forsythe, 1974).) applying the leveneTest() function . This test allowed us to

293 assess whether the variance in chemical species concentrations - reflecting chemical

294 heterogeneity - varied significantly between zones. Finally, Pearson correlation analyses

295 (Pearson, 1895; Sedgwick, 2012) were conducted on the pore water data to explore linear

296 relationships among chemical species. Two analytical levels were considered: (1)

297 correlations within individual sediment cores, and (2) correlations across all cores from the

298 same sampling zone (e.g., all cores from Z01). All statistical and geostatistical analyses were

299 performed using R version 4.2.0 (R Core Team, 2022).

300 Diffusive fluxes of sulfate, alkalinity, and calcium across the sediment–water interface were

301 calculated based on Fick's first law of diffusion using the linear concentration gradients.

302 Molecular diffusion coefficients were taken from Schulz (2006) and subsequently adjusted

303 for sediment conditions following Iversen and Jørgensen (1993). To visualize spatial patterns

304 in fluxes of sulfate, alkalinity, and calcium, we applied ordinary kriging using the gstat

305 package in R (Pebesma, 2004). First, empirical variograms were calculated from spatially

306 referenced flux measurements. Several theoretical variogram models (spherical,

307 exponential, Gaussian, and Matérn) were fitted and compared. The best-fitting model was

308 selected based on convergence criteria and plausibility of the sill and range parameters. This

309   model was then used to interpolate flux values across a regular spatial grid covering the

310   study area. The resulting kriging maps (Matheron, 1963) provided continuous spatial

311   representations of flux gradients and enabled the identification of heterogeneities between

312   hydrocarbon seep zones and reference sites. Visualizations were created using the ggplot2

313   package (Wickham, 2016).

314   **2.7. Sediment organic fraction**

315   Molecular-level insights into the organic geochemistry of sediments were obtained for

316   solvent-extractable OM using Fourier Transform Ion Cyclotron Resonance Mass

317   Spectrometry (FT-ICR-MS). Based on geochemical pore water profiles, a subset of 11

318   representative samples consisting of three samples from each of the three HC zones (Z01,

319   Z10, Z12) and one sample from each of the two reference zones (Ref5, Ref6) was selected

320   from the total of 50 sediment cores. For each sample, approximately 10 g of sediment were

321   freeze-dried, milled, and the organic content was extracted using a Soxhlet extractor

322   following a procedure described by Poetz et al. (2014). The extraction was performed with a

323   solvent mixture composed of dichloromethane and methanol (v/v = 99:1) at 40 °C for 24

324   hours. The extracts were then analyzed at ultra-high mass resolution using a Bruker Daltonik

325   Solarix 12T FT-ICR-MS. Ionization was carried out using an Apollo II ESI source and an APPI-II

326   source (all from Bruker Daltonik GmbH, Bremen, Germany).

327   For electrospray ionization (ESI−), nitrogen was used as the nebulizing gas at a flow rate of

328   4 L min^{-1} at 220 °C and a pressure of 1.4 bar. The capillary voltage was set to 3000 V, and the

329   collision-induced dissociation (CID) voltage was 60 V. The samples were infused at a flow

330   rate of 2.5 μL min^{-1} using a Hamilton syringe pump. The spectra were recorded in

331   broadband mode using 8-megaword data sets. The ion accumulation time was 0.05 s, and a

332   total of 200 scans were collected into the mass spectrum, covering a mass-to-charge ratio

333   (m/z) range of 150–1000. For atmospheric pressure photoionization (APPI+), nitrogen was

334   used as the nebulizing gas at a flow rate of 3 L min^{-1} at 210 °C and a pressure of 12.3 bar.

335   The capillary voltage was set to - 1000 V, and the CID voltage was 30 V. The samples were

336   infused at a flow rate of 20 μL min^{-1} using a Hamilton syringe pump. The spectra were

337   recorded in broadband mode using 8-megaword data sets. The ion accumulation time was

338   0.05 s, and a total of 300 scans were collected into the mass spectrum, covering an m/z

339   range of 147–1500.

340   The resulting spectra were internally recalibrated (quadratic) with a standard deviation

341   error of < 0.02 ppm, and only m/z values with a signal-to-noise ratio > 9 were exported for

342   formula assignment. Formula assignment was performed using a combination of Bruker

343   Analysis and Microsoft Excel, considering the isotopes ^{12}C and ^{13}C and the elemental ranges

344    $C_xH_yN_{0-2}O_{0-10}S_{0-2}Na_{0-1}$. The mass tolerance was set to 5 ppm.

3. Results

3.1. Methane and carbon dioxide concentrations and cell abundances

347   All samples contain measurable methane concentrations, ranging from 0.08 to 19.79 μM.

348   While samples from reference sites contain less than 5 μM of methane, higher

349   concentrations are restricted to few samples from HC-affected sites, all located deeper than

350   100 cm below seafloor (cmbsf). CO_2 was detectable in all samples, with concentrations

351   ranging from 29 μM to 512 μM, without any site-specific trend (Supplementary Fig. S1). This

352   is likely due to carbonate buffering, with dissolved CO_2 equilibrating with bicarbonate and

353   carbonate in pore water at both HC-affected and reference sites. In both cases, low gas

354   concentrations prevented measurement of their stable isotopic signatures.

355   Total cell counts are approximately 10^7 cells × cm³ across all sediment cores, with no

356   significant variation with depth (Supplementary Fig. S2). The mean deviation of cell counts

357   within samples is around 12%.
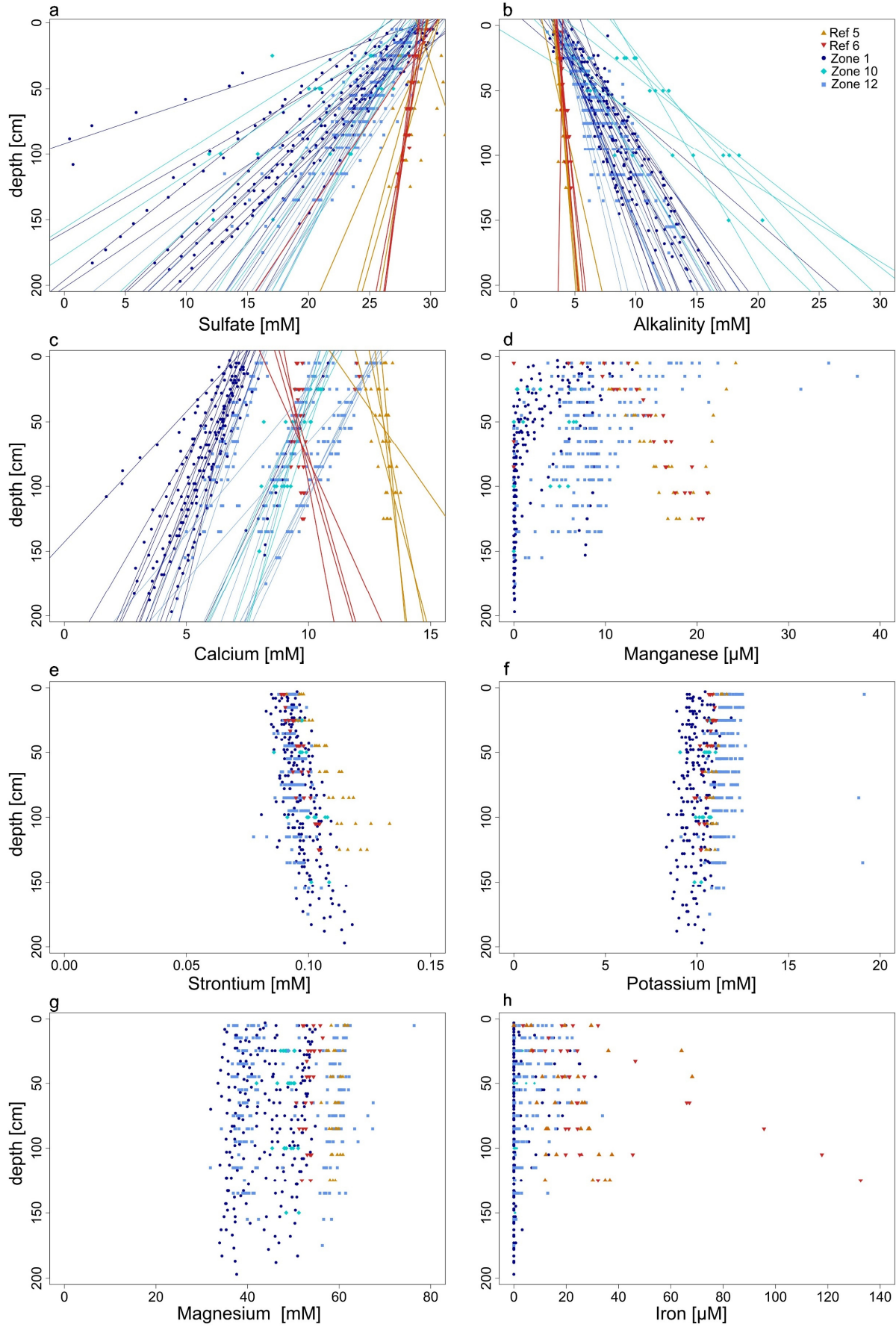
Figure 2: Pore-water profiles for some representative parameters. The profiles for sulfate concentrations (a),

360   alkalinity (b), and calcium (c) show both data points and regression lines ($R^2 > 0.8$). The regression lines for HC-

361   affected zones (Zone 1, Zone 10, Zone 12) show steeper gradients compared to those from reference zones

362   (Ref 5, Ref 6). The profiles for magnesium (d), strontium (e), potassium (f), magnesium (g), and iron (h) are

363   shown as data points due to the insufficient R^2 value of their respective regression lines.

364   **3.1. Pore water profiles**

365   Both sulfate and alkalinity concentrations exhibit strong linear decreasing and increasing

366   trends ($R^2 \geq 0.85$) with depth (Figs. 2a and 2b), respectively. The gradients are steeper in the

367   HC-affected zones compared to reference zones. Based on linear extrapolation, sulfate

368   depletion would be reached at ca. 3 and 12 mbsf in HC and reference zones, respectively.

369   Sulfide concentrations are below the detection limit (1 µM) in all cores from reference zones

370   and in most of the cores from Z12 (only 2 out of 17 cores have detectable sulfide;

371   Supplementary Fig. S3). In contrast, in most cores from Z01 (12 out of 15) and Z10 (4 out of

372   7), sulfide concentrations increase with depth.

373   In the reference zones concentrations of pore water Ca^{2+} increase with depth (Fig. 2c,

374   Supplementary Fig. S3), but decrease in the HC-affected zones. For Mn^{2+} concentrations also

375   increase with depth in the reference zones (Fig. 2d, Supplementary Fig. S4). In most of the

376   cores from HC-affected zones, Mn^{2+} pore water profiles   show a decreasing trend with

377   depth, but with distinct patterns, of which each one is predominant in a different sampling

378   zone: (1) in Z01 many profiles show concentrations decreasing from ca. 15 µM at the SWI to

379   near zero at ca. 75 cmbsf; (2) in Z12 concentrations decrease from ca. 15 µM at the SWI but

380   then stabilize around 5 µM at 1 mbsf; (3) in Z10 and Z12 some concentrations profiles

381   remain constant around 7 mM throughout depth.

382   Pore water concentrations for Cu^{2+}, Si^{4+}, Zn^{2+}, Mg^{2+} and K^+ remain almost unchanged in with

383   depth in both HC-affected and reference zones (Figs. 2e-2g, Supplementary Figs. S4-S5),

384   whereas Sr^{2+} concentrations increase in cores from both HC-affected zones and reference

385   zones, but more pronounced for the latter (Fig. 2e). Dissolved Fe^{2+} is rarely detectable in

386   cores from the HC-affected zones and falls below detection limit within the upper 1 mbsf

387   (Fig. 2h). In most cores from reference zones, pore water Fe^{2+} is detectable and

388   concentrations increase with depth. Ba^{2+} was measurable only in few cores from Z01, with

389   concentrations increasing with depth (Supplementary Fig S4). With few exceptions, Ni^{2+} and

390   As^{2+} remain below the detection limit in all samples at all depths.

391   **3.2. Statistical analyses of inter- and intrazonal variations**

392   *3.2.1. Comparative analysis of pore water geochemistry*
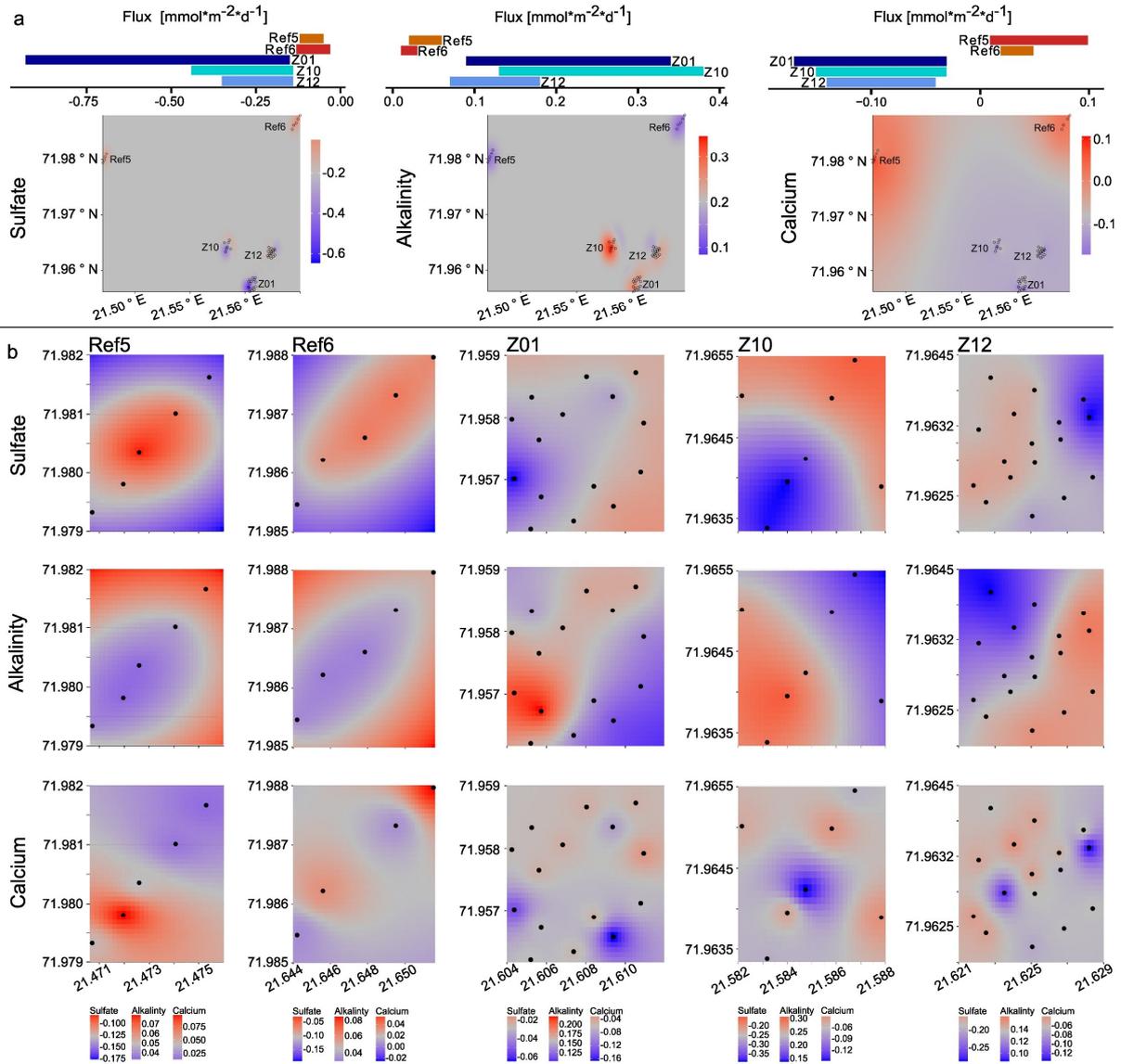
393

394   **Figure 3. Spatial variability and flux patterns of sulfate, alkalinity, and calcium across different zones.** (a) Bar

395   plots show the mean areal fluxes (mmol m^{-2} d^{-1}) of sulfate (left), alkalinity (middle), and calcium (right) at the

396   five zones (Ref5, Ref6, Z01, Z10, Z12). Kriging-interpolated maps illustrate the spatial distribution of these

397   fluxes across the study area. Color gradients indicate the direction and magnitude of fluxes. (b) Detailed kriging

398   maps of sulfate (top row), alkalinity (middle row), and calcium (bottom row) fluxes at each zone. Each column

399   corresponds to one zone, showing localized spatial variability in solute fluxes. Black dots indicate the sampling

400   sites.

401 The Mann-Whitney U tests (Mann and Whitney, 1947) confirmed statistical significance for

402 steeper sulfate and alkalinity gradients (Fig. 2, Supplementary Table S2) in HC-affected

403 zones (p_{SO4} = 3.86E-10, p_{alk} = 2.74E-05); opposite trends in Ca^{2+} profiles (p_{Ca} = 1.40E-04); and

404 different pore water gradients in Mn^{2+} concentrations (p_{Mn} = 5.38E-06), assuming linear

405 profiles which in some cases did not provide the best fit. (Fig. 2, Supplementary Fig. S4 and

406 porewater profile descriptions in Section 3.1). The results for manganese should therefore

407 be considered as approximations.

408 The Brown-Forsythe tests (Brown and Forsythe, 1974) further confirmed that the variance

409 for pore water SO_4^{2-}, alkalinity, Ca^{2+}, and Mn^{2+} gradients is smaller within reference zones

410 (all p-values < 0.05, Supplementary Table S3) than within HC-affected zones (Fig. 2). In

411 addition, a comparison of the variances across individual HC zones and reference zones

412 indicates significant differences in most instances.

413 Kriging plots for sulfate, alkalinity and calcium fluxes (which are proportional to their

414 gradients) enabled the visualization of spatial variations over the entire study area and

415 within the sampling zones (Fig. 3). The resulting patterns of variability align with previous

416 statistical tests and highlight the different spatial heterogeneity between reference and HC-

417 affected areas, with notably a stronger variability among those exposed to seepage.

418 *3.2.2. Pore water species within and across cores*

419 We also performed intra- and intervariation analyses, i.e. we investigated the correlation of

420 chemical species within each core using Pearson Correlation (Pearson, 1895; Sedgwick,

421 2012). We found a strong correlation (average |r| > 0.86) between sulfate, alkalinity and

422 calcium and, to a lesser extent (average |r| > 0.66) with manganese in almost every

423 individual core from HC zones. In contrast, within reference zones, we only found

424 correlations between alkalinity and sulfate (average r > -0.76) as well as alkalinity and

425 manganese (average r > 0.86) (Supplementary Table S4).

426 To determine whether concomitant biogeochemical processes may occur in different cores,

427 we assessed the correlation between pore water gradients for each of the 5 sampling zones

428 separately, resulting in 10 combinations of alkalinity, sulfate, manganese, calcium, and

429 sulfide. For cores from reference zones, a negative correlation between sulfate and

430   alkalinity was observed (r = -0.80 and -0.85 for Ref5 and Ref6). In addition, for Ref5,

431   additional correlations were found between sulfate and manganese (r = -0.99), alkalinity

432   and calcium (r = -0.86) and alkalinity and manganese (r = 0.78). For cores from the three HC

433   HC zones, no significant correlations (r < 0.7) were found between geochemical species,

434   except at Z10 between sulfate and alkalinity (r = - 0.89), alkalinity and sulfide (r = 0.77)

435   (Supplementary Table S4).

436   *3.2.3. XRF elemental concentrations of the sediment inorganic fraction*

437   CaO and SO_3 concentrations are significantly higher (Mann-Whitney U test, $p < 0.05$) in

438   sediments from HC-affected than reference zones. Despite similar behavior as alkaline-earth

439   elements, Ba ($p = 0.11$) and Sr ($p = 0.17$) were only slightly more abundant in sediments

440   exposed to seepage. Conversely, the relative abundance of Fe_2O_3, P_2O_5, Ti, Cr, and Zn is

441   higher ($p < 0.05$) in cores from reference zones, while Al ($p = 0.06$), Ni ($p = 0.05$), Mn ($p =$

442   0.12), and V ($p = 0.05$) show a tendency towards higher relative abundances. The loss on

443   ignition (LOI) is significantly higher ($p < 0.05$) in cores from reference zones.
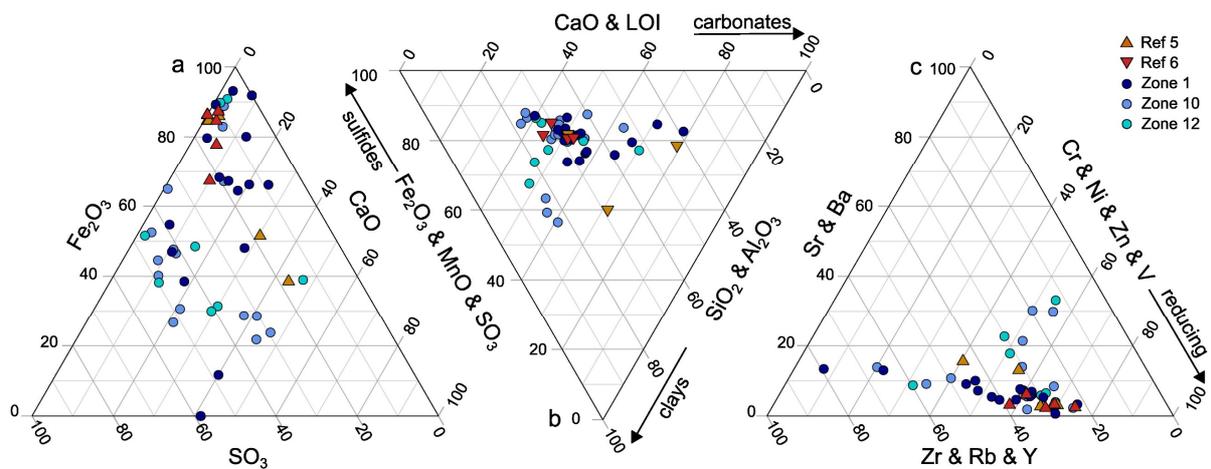
444

445   **Figure 4. Ternary diagrams showing the relative proportions of selected major and trace elements in solid**

446   **phase sediments from hydrocarbon HC zones and reference zones.** (a) Major elements: Fe_2O_3–SO_3–CaO, (b)

447   major elements grouped by associated mineral fractions: CaO and LOI (carbonate), Fe_2O_3 and MnO and SO_3

448   (sulfide), and SiO_2 and Al_2O_3 (clay), and (c) trace elements grouped by geochemical behavior: Cr, Ni, Zn and V

449   (redox-sensitive), Sr and Ba (calcite-, barite-associated), and Zr, Rb and Y (conservative). Each symbol

450   represents an individual sample. HC zones (blue colors) and reference zones (red colors) largely overlap, the

451   scatter in the HC zones is noticeably larger, indicating a greater variance.

452   Significant differences ($p < 0.05$) revealed by the Brown-Forsythe variance homogeneity test

453   included Ba and SO_3 concentrations at seepage and reference zones, highlighting higher

454   variance among cores from HC-affected zones. Variance in CaO concentrations appeared

455   non-significant ($p = 0.09$). Major and trace element in ternary diagrams (Fig. 4) confirm this,

456   as the variance (scatter) is noticeably greater in the HC zones compared to the reference

457   zones. Despite considerable overlap, this observation is consistent with the results of the

458   Brown-Forsythe test, illustrating the lower variance across samples from reference zones

459   compared to HC zones. This pattern is further supported by PCA of major and trace

460   elements (Supplementary Figs. S6–S7), where samples from HC zones show greater

461   dispersion along the first principal component (60.7% and 59.8% variance explained,

462   respectively), indicating higher variability in both major and trace element composition.

463   **3.3. Organic compound classes across sampling zones**

464   The number of mass spectrometry signals and their distribution across different compound

465   classes (e.g., pure HCs, HCs with O, N, and S atoms), measured in both ionization modes

466   (APPI+ and ESI-) and analyzed in various data representations, appear very similar for both

467   seepage and reference sites. Atomic H/C and O/C ratios derived from assigned molecular

468   formulas showed no significant differences between seep and reference sites. Additionally,

469   the degree of unsaturation (i.e. double bond equivalent, DBE) relative to the number of

470   carbon atoms does not show significant variations in the relative abundance of different

471   compound classes or noticeable differences across sampling sites (Fig. 5, Supplementary Fig.

472   8).

473   Specific molecular signatures indicative of microbial biomass (e.g. hopanoids) and degraded

474   OM (e.g. humic acids) are also comparable across sampling zones (Fig. 5). Similar to total cell

475   counts, molecular clusters assigned to hopanoid-derived compounds (typically around 6–8

476   DBE and ~30 carbons) occur in similar abundance at all sites, suggesting comparable

477   microbial population sizes. Likewise, signals corresponding to fatty acids (low DBE, low

478   number of carbons), which can be interpreted as cell remnants or necromass, are evenly

479   distributed. Finally, aromatic compounds which are typically associated with humic

480   substances from highly degraded and refractory OM, are equally present in sediments from

481   all sampling zones. Signatures of seepage-related hydrocarbons, including saturated alkanes

482   and polyaromatic hydrocarbons typically associated with migrated oil and gas, were not

483   detected.
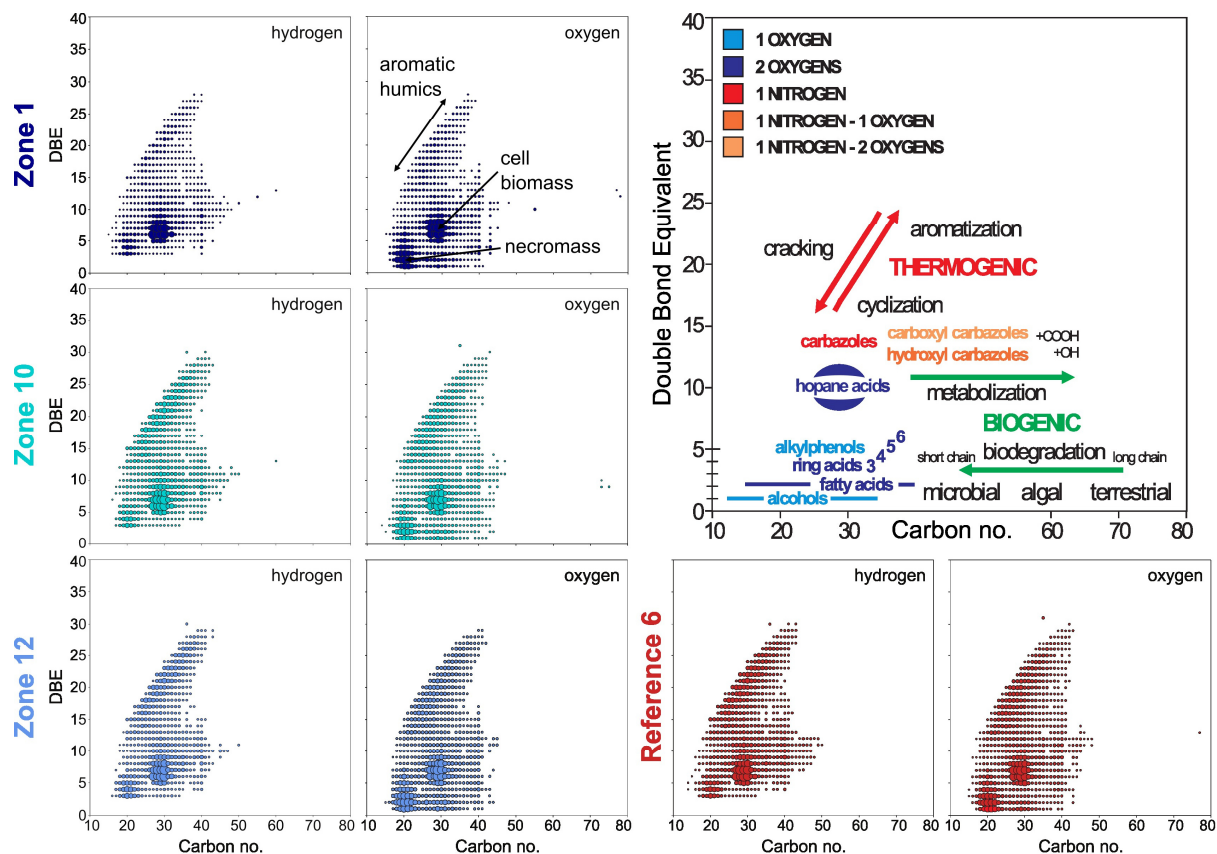
484

485   **Figure 5. Diagrams for molecular polar compounds identified by FT-ICR-MS in APPI+ mode** in sediment

486   extracts from the three hydrocarbon HC zones and one reference zone. (From left to right) Double bond

487   equivalents (DBE) plotted against carbon number for compounds containing hydrogen and oxygen, and

488   simplified interpretative framework of some molecular classes (e.g. aromatic acids, hopane acids,

489   alkylphenols) and the expected shifts related to biogenic (e.g. microbial degradation) vs. thermogenic (e.g.

490   cracking, aromatization) processes.

491   **4. Discussion**

492   In the SW Barents Sea, sediments are particularly organic-lean, with TOC values below 0.5 %

493   (Knies and Martinez, 2009). This low organic content enables the detection of discrete HC

494   seeps, as even a slight supply of electron donors can result in a direct increase in the

495   metabolic activity of HC-degrading microbial populations (Joye, 2020). This increase in

496   metabolic activity, along with the resulting geochemical redox changes, can be distinguished

497   from the background signal corresponding to pristine conditions at the seabed. In

498   comparison, any microbial or geochemical signal arising from inconspicuous HC seepage in

499 organic-rich environments would be obscured by ongoing OM breakdown, hampering

500 discrimination of specific microbial populations or metabolic pathways involved in the

501 degradation of discrete HCs.

502 **4.1. Organic signatures of potentially active seepage remain elusive**

503 At seepage sites, we expected a greater diversity and higher concentrations of oxygen-

504 containing compounds in the FT-ICR-MS mass spectra due to the formation of aromatic-ring

505 radicals and by-products (e.g. alcohols, organic acids) during microbial HC degradation

506 (Radovic and Silva, 2025). In sediments not exposed to seepage, these compounds should

507 be less abundant, with overall a lower proportion of oxygenated components. However,

508 because seepage and reference sites showed similar compound class distributions (Fig. 5;

509 Supplementary Fig. S8), our data suggest that HCs had already been degraded at sediment

510 depths below the reach of our cores, or converted into compounds with chain lengths that

511 are too short for FT-ICR-MS detection. Instead, the FT-ICR-MS analysis only captured the

512 background signal of the subseafloor sediments (i.e. biomass, necromass, organic residues),

513 the corresponding compound class concentrations being consistent with similar microbial

514 cell counts across seepage and reference sites (Supplementary Fig. 2). Thus, the suitability of

515 this classical oil (and gas) analytical tool (Marshall and Rodgers, 2004) appears to be limited

516 in the context of inconspicuous seepage, indirectly supporting our basic assumption of

517 inconspicuous HC seepage in the HC-affected zones, without any indication for increased

518 microbial biomass at seep sites.

519 **4.2. Hydrocarbon seepage shapes redox zonation with precipitation of carbonate and**

520 **sulfide minerals**

521 Marine sediments exhibit a clear redox zonation, ranging from the aerobic respiration zone

522 near the surface, transiting through the nitrate, Mn^{4+} and Fe^{3+} reduction zones to the sulfate

523 reduction zone and methanogenesis (Froelich et al., 1979; Jørgensen and Kasten, 2006). In

524 the sulfate reduction zone, sulfate acts as the electron acceptor leading to the production of

525 hydrogen sulfide, bicarbonate, and water. The increase of these compounds in the pore

526 water promotes precipitation of carbonates (e.g. calcite) and sulfide minerals (e.g., pyrite)

527 (Smrzka et al., 2020; Smrzka et al., 2024; Lin et al., 2016; Peckmann et al., 2001).

528   Consequently, the incorporation of calcium, magnesium, strontium, iron, manganese, and

529   trace elements (e.g., Cu, Ni, Zn) into these minerals leads to their depletion in pore water

530   and enrichment in the sediment's inorganic fraction (Smrzka et al., 2019; Schippers and

531   Jørgensen, 2001).

532   Both sediment geochemistry (Fig. 4, Supplementary Figs. S6-S7) and pore water analyses

533   (Fig. 2, Supplementary Figs. S3-S5) confirmed the presence of diagenetic carbonates in

534   sediments from HC zones. On the one hand, CaO, MgO, and Sr abundances increased in the

535   solid phase. On the other hand, pore water Ca^{2+} concentrations decreased while alkalinity

536   simultaneously increased with depth (Fig. 2). In contrast, Mg^{2+} and Sr^{2+} concentrations in

537   pore water remained largely unchanged. Notably, incorporation of Mg^{2+} and Sr^{2+} into

538   carbonate minerals is kinetically restricted compared to Ca^{2+} (Knight et al., 2023; Alkhatib et

539   al., 2022) and, as carbonate precipitation could occur over relatively short time periods (i.e.

540   during active seepage), substitution by pore water Mg^{2+} and Sr^{2+} appeared incomplete, thus

541   their concentrations remained almost unchanged. Although methane-derived carbonates

542   are typically high-Mg calcites or aragonite, we infer that the diagenetic carbonates in our

543   study are likely low-Mg calcites. Alternatively, the recrystallization of metastable carbonate

544   phases (e.g. aragonite) would release Sr^{2+} into the pore water (Hoareau et al., 2010). In

545   contrast to the HC zones, pore water alkalinity, Ca^{2+} and Sr^{2+} concentrations increase with

546   depth at the reference sites, while CaO and Sr contents remain low in the solid phase (Fig. 2,

547   Supplementary Fig. S3). These trends indicate that precipitation and dissolution of

548   carbonate minerals occurred (Schneider et al., 2006; Bach, 2024; Hoareau et al., 2010;

549   Smrzka et al., 2019) under seepage and non-seepage conditions, respectively.

550   Although barium (Ba^{2+}) can theoretically substitute for Ca^{2+} in carbonate minerals, its larger

551   ionic radius and strong affinity for sulfate typically limit its incorporation. Instead, Ba^{2+}

552   precipitates as barite ($BaSO_4$), which tends to dissolve under sulfate-reducing conditions

553   (Carter et al., 2020; Von Breymann et al., 1992). Indeed, Ba^{2+} was detectable in pore water

554   in only a few cores from HC-affected Zone 1 (Supplementary Fig. S4), where concentrations

555   increased with depth. This pattern suggests localized barite dissolution, likely triggered by

556   reducing conditions and upward fluid flow. Consistently, solid-phase data show elevated

557   Ba^{2+} concentrations in HC-affected zones relative to reference sites (Fig. 4, Supplementary

558   Tables S2), indicating barite accumulation through biogeochemical processes linked to HC

559   seepage. These observations highlight the dynamic interplay between sulfate availability,

560   redox zonation, and mineral precipitation at seepage sites, promoting barite formation but

561   also sulfide mineralization.

562   At seepage sites, linear profiles in pore water sulfide revealed upward diffusion

563   (Supplementary Fig. S3) and, given the low sulfate reduction rates previously measured in

564   the corresponding interval (Schnabel et al., 2025), this sulfide likely originates from deeper

565   sediment layers. When reactive metals, such as Fe^{2+}, Mn^{2+}, and other trace metals dissolved

566   in pore water, meet with ascending sulfide, precipitation of metal sulfides occurs,

567   contributing to an accumulation of redox sensitive metals and sulfur in the solid phase. This

568   is in line with observations from e.g. seeps sites in Guaymas basin (Kars et al., 2025). At

569   reference sites, dissolved sulfide is absent while Fe^{2+} and Mn^{2+} concentrations increase in

570   the pore water (Fig. 6, Supplementary Fig. S3, Supplementary Fig. S4) , suggesting that

571   anaerobic respiration of solid-phase Fe(III) and Mn(IV) oxides prevails over sulfate reduction

572   and that precipitation of metal sulfides does not take place, at least not on a quantitatively

573   significant level. Because higher pore water sulfide concentrations in our samples generally

574   correlate with elevated sulfur (i.e. SO_3) (Fig. 6) concentrations in the solid phase, sulfide

575   precipitation and sulfur accumulation allow to distinguish seepage sites from reference

576   sites, where they remain systematically low. This further demonstrates that local differences

577   in sulfide production or flux rates, as well as metal availability, may result from seepage in

578   the sediment.
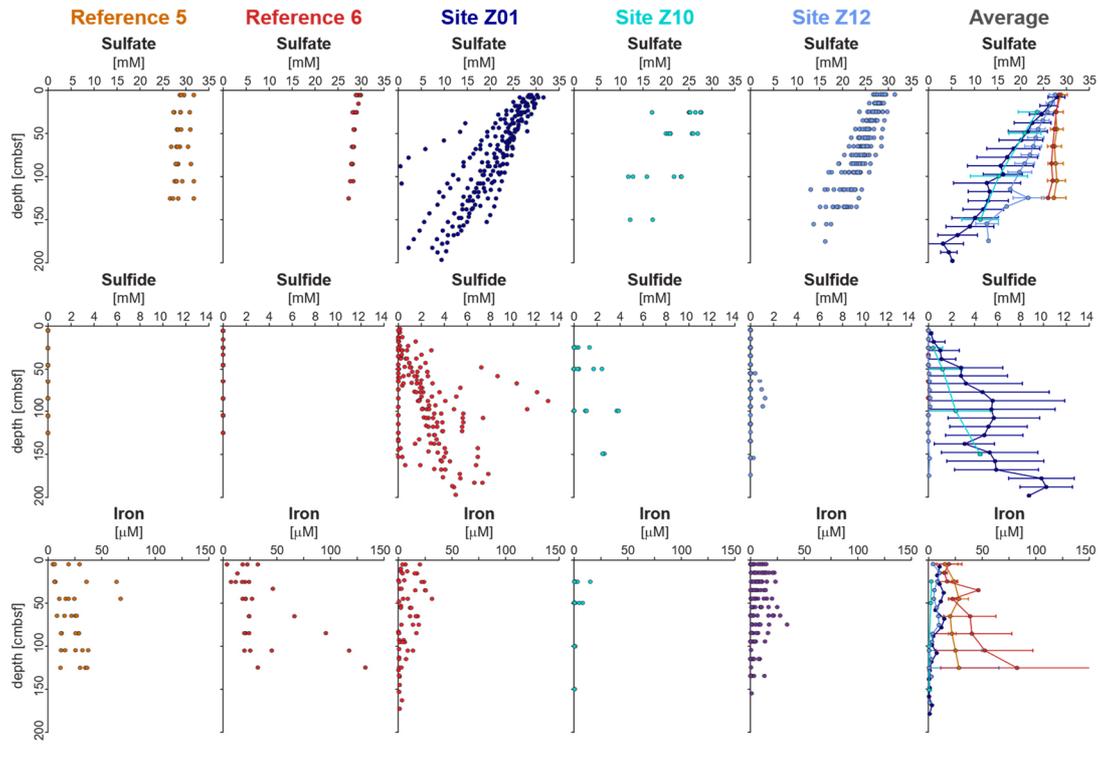
Figure 6. Porewater profiles of sulfate, sulfide, and dissolved iron across five sites, including site averages. In seep-affected cores, iron concentrations decrease where sulfide increases, indicating removal of reactive iron through sulfide precipitation. Sulfate generally decreases with depth across all sites. Error bars represent site-specific averages where applicable.

Besides major element dynamics, HC seepage also alters biogeochemical cycling of trace metals through its influence on redox zonation and authigenic mineral formation, thereby exerting control on their mobility or retention in the sediment column. Trace element incorporation into sulfide minerals vary between oil- and methane-dominated seep environments, with higher concentrations of elements like Mn, Mo, Cu, and Zn often observed in oil seep pyrites (Smrzka et al., 2024). At both seepage and reference zones, redox-sensitive trace metals (e.g. Zn, Ni, and V; Cr to a lesser extent) can be transported in solution upward from deeper sediment layers and precipitate locally depending on sulfate reduction and other redox-dependent activities. At seepage sites, methanotrophic sulfate reduction and AOM-driven processes enhance neoformation of sulfides and carbonates which act as sinks for trace metals at seep sites, in particular pyrite (Smrzka et al. (2019); Smrzka et al. (2024); Miao et al. (2022). In contrast, lower SR activity and lesser mineral precipitation at reference sites allow trace elements to continuously diffuse upward and be captured under suboxic conditions via adsorption or precipitation as iron (oxyhydr)oxides.

598   Altogether, despite similar concentrations in the pore fluid across sampling sites

599   (Supplementary Table S2), the degree and depth of occurrence of sulfate reduction govern

600   whether dissolved metal ions are sequestered in specific geochemical zones or bypass the

601   redox gradient. Nevertheless, trace metal concentrations may also vary with redox

602   gradients, precipitation kinetics, and phase-specific affinities (Smrzka et al. (2019),

603   hampering the use of pore water or solid phase concentration as a proxy for HC seepage.

604   Hence, a combined assessment of pore water geochemistry, redox zonation, and authigenic

605   minerals offers a more suitable approach for seepage characterization. Although our bulk

606   sediment geochemical data do not specifically target sulfide mineral phases, these findings

607   highlight the potential of geochemical signatures to record different seepage types.

608   4.3. Pore water fluxes and diagenetic minerals reflect the dynamics of transient seepage

609   Linear profiles for pore water alkalinity, SO_4^{2-}, and Ca^{2+} suggest no net turnover within the

610   sampled sediment interval (Schulz, 2006). This stands in contradiction with our observations

611   of the solid-phase geochemistry, which is indicative of carbonate and sulfide mineral

612   formation in HC-affected zones. We suggest that the sulfate-methane transition zone

613   (SMTZ), where most sulfide and carbonate precipitation occur, may have undergone

614   temporal and spatial depth fluctuations, driven by variations in HC flux over time. Such

615   fluctuations are well-documented and influenced by multiple factors, including

616   sedimentation rate, temperature, OM availability (Dale et al., 2008) and hydrostatic

617   pressure, which in the Barents Sea is particularly shaped by glacial-interglacial dynamics

618   (Argentino et al., 2021; Nickel, 2013).

619   In the Barents Sea, low sedimentation rates combined with extensive glacial history are

620   inferred to have shaped SMTZ dynamics. During the Last Glacial Maximum (~20 ka),

621   grounded ice sheets prevented seawater sulfate diffusion into the sediment in the Barents

622   Sea (Andreassen et al., 2008; Siegert et al., 2001), shifting the SMTZ upward. Following

623   deglaciation (~14 ka) (Elverhøi et al., 1993), seawater reoccupied the seafloor, restoring

624   sulfate supply and initiating a progressive downward migration of the SMTZ. Processes such

625   as gas hydrate dissociation and associated methane release during ice retreat (Nickel et al.,

626   2013) further enhanced these dynamics. Comparable patterns have been observed

627 elsewhere in the Barents Sea, where post-glacial rebound and HC flux variations have

628 caused significant SMTZ fluctuations (Argentino et al., 2021).

629 The occurrence of diagenetic carbonates and sulfides resulting most probably from past

630 AOM processes at the (paleo)SMTZ are therefore best understood as products of these

631 historical boundary conditions. Their accumulation in the sediment, in combination with

632 present-day linear pore water profiles, suggests that the system currently reflects a stage of

633 subdued seepage activity, and consequently deeper SMTZ. Thus, the present-day mineral

634 assemblage provides a cumulative archive of past seepage episodes rather than a snapshot

635 of ongoing processes, highlighting a key limitation of interpreting solid-phase geochemistry

636 alone. Although an increased presence of carbonates and sulfides may be indicative of past

637 redox conditions and fluid flow, these minerals cannot reliably distinguish active from relict

638 seepage. Integration with pore water profiles and other dynamic indicators remains

639 essential to reconstruct seepage history and assess present-day activity.

640 Overall, our findings align with typical mineralogical signatures of weak HC seeps, commonly

641 with carbonate (CaO) contents of 1-3 wt% (Rovere et al., 2020; Karaca et al., 2010) and

642 sulfur (SO_3) concentrations below 1 wt % (Fischer et al., 2012), thereby matching our

643 seepage site values (i.e. 2.1 wt% CaO, 0.8 wt% SO_3). The reference sites or our study exhibit

644 values (i.e.1.5 wt% CaO, 0.2 wt% SO_3) that are consistent with background diagenesis

645 typically observed in non-seep environments (1–2 wt% CaO, <0.2 wt% SO_3) (Fischer et al.,

646 2012; Karaca et al., 2010). Thus, we observe that carbonate and sulfide enrichments

647 documented in Barents Sea sediments represent the imprint of past seepage episodes,

648 whereas present-day pore water profiles reflect a current state of low, or absent, HC flux

649 within the sampled interval.

650 **4.4. Fine-scale heterogeneity characterizes weak hydrocarbon seepage**

651 The HC zones are affected by inconspicuous, diffuse seepage with very low sulfate flux rates

652 below 1 mmol × m^{-2} × d^{-1} (Fig. 3). Typical fluxes at seeps range from 1–10 mol × m^{-2} × d^{-1} for

653 high flux seeps, e.g. Coal Oil Point Seep Field, Santa Barbara, California (Padilla et al., 2019),

654 and 0.1–1 mol × m^{-2} × d^{-1} for moderate flux seeps, e.g. North-western Black Sea (Hu et al.,

655 2012). Since seepage-induced biogeochemical processes, like AOM and concomitant

656 carbonate precipitation, predominantly occur below our sampling depth range (Schnabel et

657 al., 2025), their effects can be detected only indirectly. For instance, the steeper sulfate

658 gradients observed in the HC zones compared to the reference zones (Fig. 3, Supplementary

659 Fig. S3) suggest increased sulfate reduction rates due to HC supply from below. Geochemical

660 fluxes at the seepage sites show considerable variability across individual cores (Fig. 3),

661 which is considered a typical feature of seep environments inherent to localized differences

662 in fluid flow, microbial activity, or redox conditions (Pop Ristova et al., 2015; Foster et al.,

663 2015; Schnabel et al., 2025). In contrast, reference sites present rather uniform conditions,

664 as they primarily reflect sedimentation, OM input and diffusion at the sediment-water

665 interface rather than seepage.

666 In addition to variable fluxes reported for cores from seepage sites, the pattern of

667 interconnected geochemical parameters also differs on a spatial scale (Supplementary Table

668 S4). While a single pore water species may correlate in all 50 individual cores (e.g. sulfate

669 concentrations and alkalinity), ratios between parameters appear to be different for each

670 core across different HC-affected sites, and even within each individual seepage site

671 sampled. This suggests that, even though similar microbial processes (e.g. denitrificationiron

672 reduction, sulfate reduction), can be expected to take place throughout the sampled area,

673 their degree of intensity and interactions vary on a small spatial scale, leading to

674 considerable local differences both within and between HC zones. In contrast, such

675 correlations are much better both within and across cores from reference sites (Fig. 5),

676 indicating more homogeneous and predictable diagenetic conditions.

5. Conclusions

678 This study elucidates the geochemical and mineralogical imprints of inconspicuous HC

679 seepage on near-seafloor sediments in the southwestern Barents Sea. Extremely low

680 element fluxes with often complete degradation of HCs in sediment layers below the

681 sampling depth of this study posed significant challenges in the detection of active seepage,

682 providing an explanation. This explains why anthe FT-ICR-MS-based approach was

683 unsuccessful in identifying diagnostic organic compounds., as volatile and short-chained

684 organic compounds cannot be resolved. In contrast, inorganic geochemical signatures

685 provided indirect evidence of seepage-related reductive diagenetic processes. Elevated pore

686 water alkalinity alongside decreasing Ca^{2+} concentrations with depth, substantiated by

687 elemental enrichments in the solid phase were clear indications of carbonate precipitation.

688 In addition, pore water depletion of sulfate and manganese concomitant with increased

689 solid phase sulfide concentrations point towards formation of sulfide minerals. In summary,

690 many geochemical processes along strong seeps can also be directly or indirectly detected

691 for minor HC seeps where the HCs are metabolized below the sampling interval.

692 Pronounced spatial variability in geochemical gradients across seepage-affected sites was

693 observed, revealing local heterogeneity in fluid flow and redox conditions as a result of

694 variable seepage intensity. Otherwise, correlated geochemical parameters within single

695 cores pointed to consistent coupling with past and present biogeochemical processes.

696 Altogether, these spatial patterns underline the relevance of a targeted sampling strategy to

697 resolve geochemical heterogeneities in the shallow subseafloor, which proves essential for

698 capturing the transient nature of seepage. Fine-scale geochemical variations are easily

699 overlooked but are nonetheless crucial for understanding seep dynamics and differentiating

700 between active and past seepage processes, requiring adequate spatial and temporal

701 coverage and geostatistical techniques.

6. Data availability

703 The geochemical data is available on PANGAEA as dataset #974341 and #974346 under

704 digital object identifier https://doi.pangaea.de/10.1594/PANGAEA.974341 and

705 https://doi.pangaea.de/10.1594/PANGAEA.974346.

7. Author contributions

707 JK and RDP organized the sampling cruise. ES and JK designed the study and collected

708 samples. ES performed cell counts and analyzed pore water geochemistry under the

709 supervision of JK. XRF measurements were performed under the supervision of JS. FT-ICR-

710 MS analyses of organic extracts were carried out by KM and SP. ES analyzed the data in

711 collaboration with AV, JK and SP. ES wrote the manuscript with input and revisions from all

712 co-authors.

8. Competing interests

The authors declare that they have no conflict of interest.

9. Acknowledgements

10. Financial support

The PROSPECTOMICS Consortium

The principal investigators of the PROSPECTOMICS project are Jens Kallmeyer[1], Paul Wilmes[2], Alexander J. Probst[3], Dörte Becher[4], Thomas Rattei[5], and Rolando di Primio[6]. The project managers are Aurèle Vuillemin[1], Cédric L. Laczny[2], André R. Soares[3], and Anke Trautwein-Schult[4]. Scientists and technicians include Ellen Schnabel[1], Kai Mangelsdorf[7], Steffen Okolski[1], J. Axel Kitte[1], Benoit Kunath[2], Zainab Zafar[2], Sarah Esser[3], Anne Ostrzinski[4], Sebastian Grund[4], and Alexander Pfundner[5].

[1] GFZ Helmholtz Centre for Geosciences, Section Geomicrobiology, Telegrafenberg, 14473 Potsdam, Germany; [2]Luxembourg Centre for Systems Biomedicine, University of Luxembourg, Esch-sur-Alzette; [3]Environmental Metagenomics, Research Center One Health Ruhr of the University Alliance Ruhr, Faculty of Chemistry, University of Duisburg-Essen, Essen, Germany; [4]Department of Microbial Proteomics, University of Greifswald, Greifswald,

739   Germany; [5]Computational Systems Biology, Centre for Microbiology and Environmental

740   Systems Science, University of Vienna, Vienna, Austria; [6]Aker BP ASA, Sandvika, Viken,

741   Norway; [7]GFZ Helmholtz Centre for Geosciences, Section, Section Organic Geochemistry,

742   Telegrafenberg, 14473 Potsdam, Germany.

743   **11. References**

744   Abrams, M. A.: Significance of hydrocarbon seepage relative to petroleum generation and
745   entrapment, Marine and Petroleum Geology, 22, 457-477,
746   https://doi.org/10.1016/j.marpetgeo.2004.08.003, 2005.

747   Abrams, M. A.: Marine seepage variability and its impact on evaluating the surface migrated
748   hydrocarbon seep signal, Marine and Petroleum Geology, 121, 13,
749   https://doi.org/10.1016/j.marpetgeo.2020.104600, 2020.

750   Alkhatib, M., Qutob, M., Alkhatib, S., and Eisenhauer, A.: Influence of precipitation rate and
751   temperature on the partitioning of magnesium and strontium in calcite overgrowths,
752   Chemical Geology, 599, https://doi.org/10.1016/j.chemgeo.2022.120841, 2022.

753   Andreassen, K., Laberg, J. S., and Vorren, T. O.: Seafloor geomorphology of the SW Barents
754   Sea and its glaci-dynamic implications, Geomorphology, 97, 157-177,
755   https://doi.org/10.1016/j.geomorph.2007.02.050, 2008.

756   Argentino, C., Waghorn, K. A., Vadakkepuliyambatta, S., Polteau, S., Bunz, S., and Panieri, G.:
757   Dynamic and history of methane seepage in the SW Barents Sea: new insights from
758   Leirdjupet Fault Complex, Sci Rep, 11, 4373, https://doi.org/10.1038/s41598-021-83542-0,
759   2021.

760   Bach, L. T.: The additionality problem of ocean alkalinity enhancement, Biogeosciences, 21,
761   261-277, https://doi.org/10.5194/bg-21-261-2024, 2024.

762   Berner, R. A.: A new geochemical classification of sedimentary environments, Journal of
763   Sedimentary Research, 51, 359-365, https://doi.org/10.1306/212f7c7f-2b24-11d7-
764   8648000102c1865d, 1981.

765   Bowles, M. W., Mogollon, J. M., Kasten, S., Zabel, M., and Hinrichs, K. U.: Global rates of
766   marine sulfate reduction and implications for sub-sea-floor metabolic activities, Science,
767   344, 889-891, https://doi.org/10.1126/science.1249213, 2014.

768   Bradley, J. A., Arndt, S., Amend, J. P., Burwicz, E., Dale, A. W., Egger, M., and LaRowe, D. E.:
769   Widespread energy limitation to life in global subseafloor sediments, Sci Adv, 6, eaba0697,
770   https://doi.org/10.1126/sciadv.aba0697, 2020.

771   Brown, M. B. and Forsythe, A. B.: Robust Tests for the Equality of Variances, Journal of the
772   American Statistical Association, 69, 364-367,
773   https://doi.org/10.1080/01621459.1974.10482955, 1974.

774 Carter, S. C., Paytan, A., and Griffith, E. M.: Toward an Improved Understanding of the
775 Marine Barium Cycle and the Application of Marine Barite as a Paleoproductivity Proxy,
776 Minerals, 10, https://doi.org/10.3390/min10050421, 2020.

777 Chavez, F. P., Messié, M., and Pennington, J. T.: Marine primary production in relation to
778 climate variability and change, Annual Review of Marine Science, 3, 227–260,
779 https://doi.org/10.1146/annurev.marine.010908.163917, 2011.

780 Ciotoli, G., Procesi, M., Etiope, G., Fracassi, U., and Ventura, G.: Influence of tectonics on
781 global scale distribution of geological methane emissions, Nat Commun, 11, 2305,
782 https://doi.org/10.1038/s41467-020-16229-1, 2020.

783 Cline, J. D.: Spectrophotometric Determination of Hydrogen Sulfide in Natural Waters1,
784 Limnol Oceanogr, 14, 454-458, https://doi.org/10.4319/lo.1969.14.3.0454, 1969.

785 Dale, A. W., Aguilera, D. R., Regnier, P., Fossing, H., Knab, N. J., and Jorgensen, B. B.:
786 Seasonal dynamics of the depth and rate of anaerobic oxidation of methane in Aarhus Bay
787 (Denmark) sediments, Journal of Marine Research, 66, 127-155,
788 https://doi.org/10.1357/002224008784815775, 2008.

789 de Groot, T. R., Kalenitchenko, D., Moser, M., Argentino, C., Panieri, G., Lindgren, M.,
790 Dølven, K. O., Ferré, B., Svenning, M. M., and Niemann, H.: Methanotroph activity and
791 connectivity between two seep systems north off Svalbard, Frontiers in Earth Science, 12,
792 https://doi.org/10.3389/feart.2024.1287226, 2024.

793 Dong, H., Jaisi, D. P., Kim, J., and Zhang, G.: Microbe-clay mineral interactions, American
794 Mineralogist, 94, 1505-1519, https://doi.org/10.2138/am.2009.3246, 2009.

795 Doré, A. G.: Barents Sea Geology, Petroleum Resources and Commercial Potencial, ARCTIC,
796 48, 207-221, 1995.

797 Edenborn, H. M., Paquin, Y., and Chateauneuf, G.: Bacterial contribution to manganese
798 oxidation in a deep coastal sediment, Estuarine, Coastal and Shelf Science, 21, 801-815,
799 https://doi.org/10.1016/0272-7714(85)90074-5, 1985.

800 Eichhubl, P., Davatzes, N. C., and Becker, S. P.: Structural and diagenetic control of fluid
801 migration and cementation along the Moab fault, Utah, Aapg Bulletin, 93, 653-681,
802 https://doi.org/10.1306/02180908080, 2009.

803 Elverhøi, A. and Solheim, A.: The Barents Sea ice sheet - a sedimentological discussion, Polar
804 Research, 1, 23-42, https://doi.org/10.1111/j.1751-8369.1983.tb00729.x, 1983.

805 Elverhøi, A., Fjeldskaar, W., Solheim, A., Nyland-Berg, M., and Russwurm, L.: The Barents Sea
806 Ice Sheet - a model of its growth and decay during the last ice maximum, Quaternary
807 Science Reviews, 12, 11, https://doi.org/10.1016/0277-3791(93)90025-H, 1993.

808 Etiope, G.: Natural Gas Seepage- The Earth´s Hydrocarbon Degassing, Springer, ISBN 978-3-
809 319-14601-0, 2015.

810   Faleide, J. I., Gudlaugsson, S. T., and Jacquart, G.: Evolution of the western Barents Sea,
811   Marine and Petroleum Geology, 1, 123-150, https://doi.org/10.1016/0264-8172(84)90082-
812   5, 1984.

813   Fischer, D., Sahling, H., Nöthen, K., Bohrmann, G., Zabel, M., and Kasten, S.: Interaction
814   between hydrocarbon seepage, chemosynthetic communities, and bottom water redox at
815   cold seeps of the Makran accretionary prism: insights from habitat-specific pore water
816   sampling and modeling, Biogeosciences, 9, 2013-2031, https://doi.org/10.5194/bg-9-2013-
817   2012, 2012.

818   Foster, K. L., Stern, G. A., Carrie, J., Bailey, J. N., Outridge, P. M., Sanei, H., and Macdonald, R.
819   W.: Spatial, temporal, and source variations of hydrocarbons in marine sediments from
820   Baffin Bay, Eastern Canadian Arctic, Sci Total Environ, 506-507, 430-443,
821   https://doi.org/10.1016/j.scitotenv.2014.11.002, 2015.

822   Froelich, P. N., Klinkhammer, G. P., Bender, M. L., Luedtke, N. A., Heath, G. R., Cullen, D.,
823   Dauphin, P., Hammond, D., Hartman, B., and Maynard, V.: Early oxidation of organic matter
824   in pelagic sediments of the eastern equatorial Atlantic: suboxic diagenesis, Geochemica et
825   Cosmochimica Acta, 43, 1975-1090, https://doi.org/10.16/0016-7037(79)90095-4, 1979.

826   Gabrielsen, R. H., Faerseth, R. B., Jensen, L. N., Kalheim, J. E., and Riis, F.: Structual elements
827   of the Norwegian continental shelf, Part 1: The Barents Sea Region, NPD Bulletin, 6, 1-33,
828   1990.

829   Heggland, R.: Gas seepage as an indicator of deeper prospective reservoirs. A study based
830   on exploration 3D seismic data, Marine and Petroleum Geology, 15, 1-9,
831   https://doi.org/10.1016/S0264-8172(97)00060-3, 1998.

832   Hinrichs, K. U., Hayes, J. M., Sylva, S. P., Brewer, P. G., and DeLong, E. F.: Methane-
833   consuming archaebacteria in marine sediments, Nature, 398, 802-805,
834   https://doi.org/10.1038/19751, 1999.

835   Hoareau, G., Monnin, C., and Odonne, F.: A study of celestine equilibrium in marine
836   sediments using the entire ODP/IODP porewater data base, Geochimica et Cosmochimica
837   Acta, 74, 3925-3937, https://doi.org/10.1016/j.gca.2010.03.033, 2010.

838   Hu, L., Yvon-Lewis, S. A., Kessler, J. D., and MacDonald, I. R.: Methane fluxes to the
839   atmosphere from deepwater hydrocarbon seeps in the northern Gulf of Mexico, Journal of
840   Geophysical Research: Oceans, 117, https://doi.org/10.1029/2011jc007208, 2012.

841   Hu, T., Luo, M., Qi, Y., He, D., Chen, L., Xu, Y., and Chen, D.: Molecular evidence for the
842   production of labile, sulfur-bearing dissolved organic matter in the seep sediments of the
843   South China Sea, Water Res, 233, 119732, https://doi.org/10.1016/j.watres.2023.119732,
844   2023.

845   Huerta-Diaz, M. A. and Morse, J. W.: Pyritization of trace metals in anoxic marine sediments,
846   Geochimica et Cosmochimica Acta, 56, 2681-2702, https://doi.org/10.1016/0016-
847   7037(92)90353-k, 1992.

848   Hunt, J. M.: Petroleum Geochemistry and Geology, W.H.Freeman & Co Ltd, New York, ISBN
849   9780716724414, 1995.

850   Hvoslef, S., Christie, O. H. J., Sassen, R., Kennicutt, M. C., Requejo, A. G., and Brooks, J. M.:
851   Test of a new surface geochemistry tool for resource prediction in frontier areas, Marine
852   and Petroleum Geology, 13, 107-124, https://doi.org/10.1016/0264-8172(95)00032-1, 1996.

853   Iversen, N. and Jørgensen, B. B.: Diffusion coefficents of sulfate and methane in marine
854   sediments: Influence of porosity, Geochemica et Cosmochemica Acta, 57, 571-778,
855   https://doi.org/10.1016/0016-7037(93)90368-7, 1993.

856   Johansen, S. E., Ostisty, B. K., Birkeland, ø., Fedorovsky, Y. F., Martirosjan, V. N., Bruun
857   Christensen, O., Cheredeev, S. I., Ignatenko, E. A., and Margulis, L. S.: Hydrocarbon potential
858   in the Barents Sea region: play distribution and potential, Norwegian Petroleum Society
859   Special Publications, 2, 273-320, https://doi.org/10.1016/B978-0-444-88943-0.50024-1,
860   1993.

861   Jørgensen, B. B.: Mineralization of organic matter in the sea bed—the role of sulphate
862   reduction, Nature, 296, 643-645, https://doi.org/10.1038/296643a0, 1982.

863   Jørgensen, B. B. and Kasten, S.: Sulfur Cycling and Methane Oxidation, in: Marine
864   Geochemistry, 271-309, https://doi.org/10.1007/3-540-32144-6_8, 2006.

865   Jørgensen, B. B., Findlay, A. J., and Pellerin, A.: The Biogeochemical Sulfur Cycle of Marine
866   Sediments, Front Microbiol, 10, 849, https://doi.org/10.3389/fmicb.2019.00849, 2019.

867   Joye, S. B.: The Geology and Biogeochemistry of Hydrocarbon Seeps, Annual Review of Earth
868   and Planetary Sciences, 48, 205-231, https://doi.org/10.1146/annurev-earth-063016-
869   020052, 2020.

870   Joye, S. B., Bowles, M. W., and Ziervogel, K.: Marine Biogeochemical Cycles, in: The Marine
871   Microbiome, 623-671, https://doi.org/ 10.1007/978-3-030-90383-1_15, 2022.

872   Joye, S. B., Boetius, A., Orcutt, B. N., Montoya, J. P., Schulz, H. N., Erickson, M. J., and Lugo,
873   S. K.: The anaerobic oxidation of methane and sulfate reduction in sediments from Gulf of
874   Mexico cold seeps, Chemical Geology, 205, 219-238,
875   https://doi.org/10.1016/j.chemgeo.2003.12.019, 2004.

876   Judd, A. and Hovland, M.: Seabed fluid flow- The impact on geology, biology and the marine
877   environment, Cambridge University Press, https://doi.org/10.1017/cbo9780511535918,
878   2009.

879   Kallmeyer, J., Smith, D. C., Spivack, A. J., and D'Hondt, S.: New cell extraction procedure
880   applied to deep subsurface sediments, Limnology and Oceanography: Methods, 6, 236-245,
881   https://doi.org/10.4319/lom.2008.6.236, 2008.

882   Karaca, D., Hensen, C., and Wallmann, K.: Controls on authigenic carbonate precipitation at
883   cold seeps along the convergent margin off Costa Rica, Geochemistry, Geophysics,
884   Geosystems, 11, https://doi.org/10.1029/2010gc003062, 2010.

885 Kars, M. A. C., Pastor, L., Burin, C., and Koornneef, L. M. T.: Data report: characterization of
886 iron oxides and iron sulfides in sediments from IODP Expedition 385 Sites U1549 and U1552
887 using rock magnetism and geochemistry, in: Proceedings of the International Ocean
888 Discovery Program, Teske, A., Lizarralde, D., Höfig, T. W., and the Expedition 385 Scientists
889 (Eds.), Volume 385, 19 pp., International Ocean Discovery Program,
890 https://doi.org/10.14379/iodp.proc.385.207.2025, 2025.

891 Kasten, S. and Jørgensen, B. B.: Sulfate Reduction in Marine Sediments, in: Marine
892 Geochemistry, Springer, Heidelberg, 263-281, https://doi.org/10.1007/978-3-662-04242-
893 7_8, 2000.

894 Kim, J., Dong, H. L., Seabaugh, J., Newell, S. W., and Eberl, D. D.: Role of microbes in the
895 smectite-to-illite reaction, Science, 303, 830-832, https://doi.org/10.1126/science.1093245,
896 2004.

897 Knies, J. and Martinez, P.: Organic matter sedimentation in the western Barents Sea region:
898 Terrestrial and marine contribution based on isotopic composition and organic nitrogen
899 content, Norwegian Journal of Geology, 89, 79-89, 2009.

900 Knight, A. W., Harvey, J. A., Shohel, M., Lu, P., Cummings, D., and Ilgen, A. G.: The combined
901 effects of Mg^{2+} and Sr^{2+} incorporation during $CaCO_3$ precipitation and crystal growth,
902 Geochimica et Cosmochimica Acta, 345, 16-33, https://doi.org/10.1016/j.gca.2023.01.021,
903 2023.

904 Langrock, U., Stein, R., Lipinski, M., and Brumsack, H.-J. r.: Paleoenvironment and sea-level
905 change in the early Cretaceous Barents Sea?implications from near-shore marine sapropels,
906 Geo-Marine Letters, 23, 34-42, https://doi.org/10.1007/s00367-003-0122-5, 2003.

907 Larssen, G. B., Elvebakk, G., Henriksen, L. B., Kristensen, S.-E., Nilsson, I., Samuelsberg, T. J.,
908 Svana, T. A., Stemmerik, L., and Worsley, D.: Upper Palaeozoic lithostratigraphy of the
909 Southern Norwegian Barents Sea, Norsk Geologisk Undersøkelser, Bull., 444, 43, 2002.

910 Leifer, I., Boles, J. R., Luyendyk, B. P., and Clark, J. F.: Transient discharges from marine
911 hydrocarbon seeps: spatial and temporal variability, Environmental Geology, 46, 1038-1052,
912 https://doi.org/10.1007/s00254-004-1091-3, 2004.

913 Lin, Z., Sun, X., Peckmann, J., Lu, Y., Xu, L., Strauss, H., Zhou, H., Gong, J., Lu, H., and Teichert,
914 B. M. A.: How sulfate-driven anaerobic oxidation of methane affects the sulfur isotopic
915 composition of pyrite: A SIMS study from the South China Sea, Chemical Geology, 440, 26-
916 41, https://doi.org/10.1016/j.chemgeo.2016.07.007, 2016.

917 Mann, H. B. and Whitney, D. R.: On a Test of Whether one of Two Random Variables is
918 Stochastically Larger than the Other, The Annals of Mathematical Statistics, 18, 50-60,
919 https://doi.org/10.1214/aoms/1177730491, 1947.

920 Marín, D., Helleren, S., Escalona, A., Olaussen, S., Cedeño, A., Nøhr-Hansen, H., and Ohm, S.:
921 The Middle Jurassic to lowermost Cretaceous in the SW Barents Sea: Interplay between

922   tectonics, coarse-grained sediment supply and organic matter preservation, Basin Research,
923   33, 1033-1055, https://doi.org/10.1111/bre.12504, 2020.

924   Marshall, A. G. and Rodgers, R. P.: Petroleomics: the next grand challenge for chemical
925   analysis, Acc Chem Res, 37, 53-59, https://doi.org/10.1021/ar020177t, 2004.

926   Matheron, G.: Principles of geostatistics, Economic Geology, 58, 1246-1266,
927   https://doi.org/10.2113/gsecongeo.58.8.1246, 1963.

928   Miao, X., Feng, X., Li, J., Liu, X., Liang, J., Feng, J., Xiao, Q., Dan, X., and Wei, J.: Enrichment
929   mechanism of trace elements in pyrite under methane seepage, Geochemical Perspectives
930   Letters, 21, 18-22, https://doi.org/10.7185/geochemlet.2211, 2022.

931   Middelburg, J. J.: Reviews and syntheses: to the bottom of carbon processing at the
932   seafloor, Biogeosciences, 15, 413-427, https://doi.org/10.5194/bg-15-413-2018, 2018.

933   Nickel, J. C., di Primio, R., Mangelsdorf, K., Stoddart, D., and Kallmeyer, J.: Characterization
934   of microbial activity in pockmark fields of the SW-Barents Sea, Marine Geology, 332–334,
935   152–162, https://doi.org/10.1016/j.margeo.2012.02.002, 2012.

936   Nickel, J. C., di Primio, R., Kallmeyer, J., Hammer, Ø., Horsfield, B., Stoddart, D., Brunstad, H.,
937   and Mangelsdorf, K.: Tracing the origin of thermogenic hydrocarbon signals in pockmarks
938   from the southwestern Barents Sea, Organic Geochemistry, 63, 73-84,
939   https://doi.org/10.1016/j.orggeochem.2013.08.008, 2013.

940   Orphan, V. J., Hinrichs, K. U., Ussler, W., 3rd, Paull, C. K., Taylor, L. T., Sylva, S. P., Hayes, J.
941   M., and Delong, E. F.: Comparative analysis of methane-oxidizing archaea and sulfate-
942   reducing bacteria in anoxic marine sediments, Appl Environ Microbiol, 67, 1922-1934,
943   https://doi.org/10.1128/AEM.67.4.1922-1934.2001, 2001.

944   Padilla, A. M., Loranger, S., Kinnaman, F. S., Valentine, D. L., and Weber, T. C.: Modern
945   Assessment of Natural Hydrocarbon Gas Flux at the Coal Oil Point Seep Field, Santa Barbara,
946   California, Journal of Geophysical Research: Oceans, 124, 2472-2484,
947   https://doi.org/10.1029/2018jc014573, 2019.

948   Pearson, K.: Note on regression and inheritance in the case of two parents, Proceedings of
949   the Royal Society of London, 58, 240-242, https://doi.org/10.1098/rspl.1895.0041, 1895.

950   Pebesma, E. J.: Multivariable geostatistics in S: the gstat package, Computers & Geosciences,
951   30, 683-691, https://doi.org/10.1016/j.cageo.2004.03.012, 2004.

952   Peckmann, J., Reimer, A., Luth, U., Luth, C., Hansen, B. T., Heinicke, C., Hoefs, J., and Reitner,
953   J.: Methane-derived carbonates and authigenic pyrite from the northwestern Black Sea,
954   Marine Geology, 177, 129-150, https://doi.org/10.1016/S0025-3227(01)00128-1, 2001.

955   Poetz, S., Horsfield, B., and Wilkes, H.: Maturity-Driven Generation and Transformation of
956   Acidic Compounds in the Organic-Rich Posidonia Shale as Revealed by Electrospray
957   Ionization Fourier Transform Ion Cyclotron Resonance Mass Spectrometry, Energy & Fuels,
958   28, 4877-4888, https://doi.org/10.1021/ef500688s, 2014.

959   Pop Ristova, P., Wenzhofer, F., Ramette, A., Felden, J., and Boetius, A.: Spatial scales of
960   bacterial community diversity at cold seeps (Eastern Mediterranean Sea), ISME J, 9, 1306-
961   1318, https://doi.org/10.1038/ismej.2014.217, 2015.

962   R: A language and environment for statistical computing: https://www.R-project.org/, last
963   access: 2023-06-12.

964   Radovic, J. R. and Silva, R. C.: Ultrahigh-Resolution Mass Spectrometry Advances for
965   Biogeochemical Analysis: From Seafloor Sediments to Petroleum and Marine Oil Spills, J Am
966   Soc Mass Spectrom, 36, 7-33, https://doi.org/10.1021/jasms.4c00266, 2025.

967   Rasheed, M. A., Lakshmi, M., Rao, P. L. S., Kalpana, M. S., Dayal, A. M., and Patil, D. J.:
968   Geochemical evidences of trace metal anomalies for finding hydrocarbon microseepage in
969   the petroliferous regions of the Tatipaka and Pasarlapudi areas of Krishna Godavari Basin,
970   India, Petroleum Science, 10, 19-29, https://doi.org/10.1007/s12182-013-0245-x, 2013.

971   Rovere, M., Mercorella, A., Frapiccini, E., Funari, V., Spagnoli, F., Pellegrini, C., Bonetti, A. S.,
972   Veneruso, T., Tassetti, A. N., Dell'Orso, M., Mastroianni, M., Giuliani, G., De Marco, R., Fabi,
973   G., Ciccone, F., and Antoncecchi, I.: Geochemical and Geophysical Monitoring of
974   Hydrocarbon Seepage in the Adriatic Sea, Sensors (Basel), 20,
975   https://doi.org/10.3390/s20051504, 2020.

976   Røy, H., Kallmeyer, J., Adhikari, R. R., Pockalny, R., Jørgensen, B. B., and D'Hondt, S.: Aerobic
977   microbial respiration in 86-million-year-old deep-sea red clay, Science, 336, 922-925,
978   https://doi.org/10.1126/science.1219424, 2012.

979   Sættem, J., Rise, L., and Westgaard, D. A.: Composition and properties of glacigenic
980   sediments in the southwestern Barents Sea, Marine Geotechnology, 10, 229-255,
981   https://doi.org/10.1080/10641199109379893, 1991.

982   Schippers, A. and Jørgensen, B. B.: Oxidation of pyrite and iron sulfide by manganese dioxide
983   in marine sediments, Geochimica et Cosmochimica Acta, 65, 915-922,
984   https://doi.org/10.1016/s0016-7037(00)00589-5, 2001.

985   Schnabel, E., Vuillemin, A., Laczny, C. C., Kunath, B. J., Soares, A. R., Probst, A. J., Di Primio,
986   R., Kallmeyer, J., and the, P. C.: Influence of minor hydrocarbon seepage on sulfur cycling in
987   marine subsurface sediments, Biogeosciences, 22, 767-784, https://doi.org/10.5194/bg-22-
988   767-2025, 2025.

989   Schneider, R. R., Schulz, H. D., and Hensen, C.: Marine Carbonates: Their Formation and
990   Destruction, in: Marine Geochemistry, edited by: Schulz, H. D., and Zabel, M., Springer,
991   Berlin, Heidelberg, 311-337, https://doi.org/10.1007/3-540-32144-6_9, 2006.

992   Schulz, H. D.: Quantification of Early Diagenesis: Dissolved Constituents in Pore Water and
993   Signals in the Solid Phase, in: Marine Geochemistry, 73-124, https://doi.org/10.1007/3-540-
994   32144-6_3, 2006.

995   Sedgwick, P.: Pearson's correlation coefficient, Bmj, 345, e4483-e4483,
996   https://doi.org/10.1136/bmj.e4483, 2012.

997   Seeberg-Elverfeldt, J., Schluter, M., Feseker, T., and Kolling, M.: Rhizon sampling of
998   porewaters near the sediment-water interface of aquatic systems, Limnol Oceanogr-Meth,
999   3, 361-371, https://doi.org/10.4319/lom.2005.3.361, 2005.

1000   Sert, M. F., D'Andrilli, J., Gründger, F., Niemann, H., Granskog, M. A., Pavlov, A. K., Ferré, B.,
1001   and Silyakova, A.: Compositional Differences in Dissolved Organic Matter Between Arctic
1002   Cold Seeps Versus Non-Seep Sites at the Svalbard Continental Margin and the Barents Sea,
1003   Frontiers in Earth Science, 8, https://doi.org/10.3389/feart.2020.552731, 2020.

1004   Siegert, M. J., Dowdeswell, J. A., Hald, M., and Svendsen, J. I.: Modelling the Eurasian Ice
1005   Sheet through a full (Weichselian) glacial cycle, Global and Planetary Change, 31, 367-385,
1006   https://doi.org/10.1016/S0921-8181(01)00130-8, 2001.

1007   Smrzka, D., Lin, Z., Monien, P., Chen, T., Bach, W., Peckmann, J., and Bohrmann, G.: Pyrite-
1008   based trace element fingerprints for methane and oil seepage, Geochemical Perspectives
1009   Letters, 29, 33-37, https://doi.org/10.7185/geochemlet.2409, 2024.

1010   Smrzka, D., Zwicker, J., Bach, W., Feng, D., Himmler, T., Chen, D., and Peckmann, J.: The
1011   behavior of trace elements in seawater, sedimentary pore water, and their incorporation
1012   into carbonate minerals: a review, Facies, 65, 47, https://doi.org/10.1007/s10347-019-0581-
1013   4, 2019.

1014   Smrzka, D., Feng, D., Himmler, T., Zwicker, J., Hu, Y., Monien, P., Tribovillard, N., Chen, D.,
1015   and Peckmann, J.: Trace elements in methane-seep carbonates: Potentials, limitations, and
1016   perspectives, Earth-Science Reviews, 208, https://doi.org/10.1016/j.earscirev.2020.103263,
1017   2020.

1018   Tribovillard, N., du Châtelet, E. A., Gay, A., Barbecot, F., Sansjofre, P., and Potdevin, J.-L.:
1019   Geochemistry of cold seepage-impacted sediments: Per-ascensum or per-descensum trace
1020   metal enrichment?, Chemical Geology, 340, 1-12,
1021   https://doi.org/10.1016/j.chemgeo.2012.12.012, 2013.

1022   Viollier, E., Inglett, P. W., Hunter, K., Roychoudhury, A. N., and Van Cappellen, P.: The
1023   ferrozine method revisited: Fe(II)/Fe(III) determination in natural waters, Applied
1024   Geochemistry, 15, 785-790, https://doi.org/10.1016/s0883-2927(99)00097-9, 2000.

1025   von Breymann, M. T., Brumsack, H., and Emeis, K. C.: Depositional and Diagenetic Behavior
1026   of Barium in the Japan Sea, in: Proceedings of the Ocean Drilling Program, 127/128 Part 1
1027   Scientific Results, Proceedings of the Ocean Drilling Program,
1028   https://doi.org/10.2973/odp.proc.sr.127128-1.168.1992, 1992.

1029   Vuillemin, A., Morlock, M., Paskin, A., Benning, L. G., Henny, C., Kallmeyer, J., Russell, J. M.,
1030   and Vogel, H.: Authigenic minerals reflect microbial control on pore waters in a ferruginous
1031   analogue, Geochemical Perspectives Letters, 28, 20-26,
1032   https://doi.org/10.7185/geochemlet.2339, 2023a.

1033   Vuillemin, A., Vargas, S., Coskun, O. K., Pockalny, R., Murray, R. W., Smith, D. C., D'Hondt, S.,
1034   and Orsi, W. D.: Atribacteria Reproducing over Millions of Years in the Atlantic Abyssal
1035   Subseafloor, mBio, 11, https://doi.org/10.1128/mBio.01937-20, 2020.

1036   Vuillemin, A., Mayr, C., Schuessler, J. A., Friese, A., Bauer, K. W., Lücke, A., Heuer, V. B.,
1037   Glombitza, C., Henny, C., von Blanckenburg, F., Russell, J. M., Bijaksana, S., Vogel, H., Crowe,
1038   S. A., and Kallmeyer, J.: A one-million-year isotope record from siderites formed in modern
1039   ferruginous sediments, GSA Bulletin, 135, 504-522, https://doi.org/10.1130/b36211.1,
1040   2023b.

1041   Wickham, H.: ggplot2, 2, Use R!, Springer-Verlag, New York, 260 pp.,
1042   https://doi.org/10.1007/978-3-319-24277-4, 2016.

1043   Widdel, F., Knittel, K., and Galushko, A.: Anaerobic Hydrocarbon- Degrading
1044   Microorganisms: An Overview, in: Handbook of Hydrocarbon and Lipid Microbiology,
1045   Springer, Berlin, Heidelberg, 1997-2021, https://doi.org/10.1007/978-3-540-77587-4, 2010.

1046   Yergin, D.: The Prize: The Epic Quest for Oil, Money & Power, Free Press, ISBN
1047   9781847376466, 2009.

1048   Zhang, X., Wu, K., Han, Z., Chen, Z., Liu, Z., Sun, Z., Shao, L., Zhao, Z., and Zhou, L.: Microbial
1049   diversity and biogeochemical cycling potential in deep-sea sediments associated with
1050   seamount, trench, and cold seep ecosystems, Front Microbiol, 13, 1029564,
1051   https://doi.org/10.3389/fmicb.2022.1029564, 2022.

1052   Zhao, R. X., Xue, H. T., Lu, S. F., Greenwell, and Erastova, V.: Revealing crucial effects of
1053   reservoir environment and hydrocarbon fractions on fluid behavior in kaolinite pores, Chem
1054   Eng J, 489, https://doi.org/10.1016/j.cej.2024.151362, 2024.